ELSEVIER

Contents lists available at ScienceDirect

# **Quaternary Science Reviews**

journal homepage: www.elsevier.com/locate/quascirev



Invited paper

# A mechanistic understanding of oxygen isotopic changes in the Western United States at the Last Glacial Maximum



Clay Tabor <sup>a, \*</sup>, Marcus Lofverstrom <sup>b</sup>, Jessica Oster <sup>c</sup>, Barbara Wortham <sup>d</sup>, Cameron de Wet <sup>c</sup>, Isabel Montañez <sup>d</sup>, Alan Rhoades <sup>e</sup>, Colin Zarzycki <sup>f</sup>, Chengfei He <sup>g</sup>, Zhengyu Liu <sup>g</sup>

- <sup>a</sup> Department of Geosciences, University of Connecticut, Storrs, CT, 06269, USA
- <sup>b</sup> Department of Geosciences, University of Arizona, Tucson, AZ, 85719, USA
- <sup>c</sup> Department of Earth and Environmental Sciences, Vanderbilt University, Nashville, TN, 37240, USA
- <sup>d</sup> Department of Earth and Planetary Sciences, University of California–Davis, Davis, CA, 95616, USA
- <sup>e</sup> Climate and Ecosystem Sciences Division, Lawrence Berkeley National Laboratory, Berkeley, CA, 94720, USA
- f Department of Meteorology and Atmospheric Science, Pennsylvania State University, University Park, PA, 16802, USA
- g Department of Geography, Ohio State University, Columbus, OH, 43210, USA

#### ARTICLE INFO

# Article history: Received 21 July 2021 Received in revised form 19 October 2021 Accepted 24 October 2021 Available online xxx

Handling Editor: I Hendy

Keywords: Quaternary Climate dynamics Paleoclimate modeling Paleoclimatology North America Speleothems Stable isotopes

#### ABSTRACT

At the Last Glacial Maximum (LGM), records suggest drier conditions in the northwest United States and wetter conditions in the southwest United States relative to present-day as well as widespread changes in the isotopic composition of water. However, the mechanisms responsible for these changes remain ambiguous. Here, we explore differences in western United States hydroclimate between the LGM and preindustrial with a water isotope tracer enabled Earth System Model. We then use proxy forward models to compare simulated and recorded  $\delta^{18}O$  in speleothems. We find that the pattern of hydroclimate response in the western United States at the LGM relates to a combination of 1) increased frequency and southward shifted wintertime extratropical cyclones in the North Pacific, 2) greater rainout of moisture as it moves over the continent, and 3) reduced evaporation in the cooler LGM climate. The simulated lower  $\delta^{18}\text{O}$  of precipitation at the LGM relates predominantly to an increase in cool season moisture removal efficiency, with a secondary contribution from relatively more cool season precipitation. Both surface temperatures and North American ice sheets contribute to these hydroclimate changes at the LGM. Comparisons between  $\delta^{18}$ O from proxy forward models and speleothem records in the western United States show general agreement at the LGM, with increasing depletion moving towards the continental interior. This study highlights the similarities and differences between hydrologic and  $\delta^{18}$ O changes at the LGM and emphasizes the utility of model-proxy comparison for interpretation.

© 2021 Elsevier Ltd. All rights reserved.

## 1. Introduction

The Western United States (W-US), defined here as states west of the Rocky Mountains, is home to over 66 million people, spans 1.88 million km², and produces almost 23% of the country's gross domestic product (US Bureau of Economic Analysis, 2020, US Census Bureau, 2020). The geography and topography of the W-US encompasses a wide range of climates in a relatively confined region, with desert climate in the southwest, dry to wet

Corresponding author. E-mail address: clay.tabor@uconn.edu (C. Tabor). Mediterranean climate along the Pacific coast, semi-arid steppe land extending into the continental interior, and a variety of alpine climates along the mountain ranges (Kottek et al., 2006). Seasonal-to-interdecadal synoptic patterns of ocean-atmosphere variability in the Pacific modulate W-US precipitation (e.g., Dettinger et al., 1998), which is largely a product of extratropical cyclones during the winter, particularly along the Pacific coast (Chang et al., 2015). Inhabitants of the W-US depend on this seasonal precipitation to replenish snowpack, groundwater, and surface reservoirs for the subsequent dry summer season.

Given the significance of the W-US to food production and economics, there have been many studies on how this region will respond to anthropogenic climate change (e.g., Hamlet and

Lettenmaier, 2007; Dettinger et al., 2015; Rhoades et al., 2021). Most simulations suggest increased risk of drought and seasonal precipitation variability in the coming decades to centuries as the climatic effects of greenhouse gas emissions become more pronounced (e.g., Seager et al., 2007; Diffenbaugh et al., 2015; Swain et al., 2018). However, there remains significant uncertainty in the degree of hydrologic change regionally with warming. Furthermore, the diversity of climates in the W-US will not respond uniformly to climate change due to the variety of drivers of hydroclimate in the region. Recent work suggests similar patterns of hydroclimate change in the W-US under past and future forcing scenarios, which highlights the value in exploring past climate to understand current and future climate change (Rehfeld et al., 2020).

Evidence for a spatially varied hydroclimate response in the W-US to climate change exists in proxy records of the Last Glacial Maximum (LGM, ca. 21,000 years before present; e.g., Oster et al., 2015a, 2020; Feakins et al., 2019; Hudson et al., 2019). During this time, climate reconstructions of the W-US suggest comparatively wetter conditions in the south and drier conditions in the north. Of the many proxy archives gathered in the W-US, measurements of  $\delta^{18}$ O in cave records, known as speleothems, have proven to be particularly valuable because they can produce long, continuous records of past hydroclimate change with robust age constraints (e.g., Oster and Kelley, 2016). However, the various mechanisms that produced these  $\delta^{18}$ O signals are difficult to deconvolve and continue to be debated.

Climate model simulations have long explored this unique dipole response to understand W-US climate dynamics (e.g., Manabe and Broccoli, 1985; COHMAP Members, 1998; Oster et al., 2015a; Löfverström and Liakka, 2016; Lora et al., 2017; Lora, 2018; Morrill et al., 2018; Lofverstrom, 2020). Although many climate models configured with period appropriate boundary conditions can capture the measured pattern of hydrologic change in the W-US at the LGM (e.g., Kageyama et al., 2021), debate remains as to the underlying dynamics responsible for the spatial pattern of wet and dry. A long-standing hypothesis suggests that southward-displaced westerlies led to the shift in W-US moisture at the LGM (e.g., COHMAP Members, 1998). More recently, alternative hypotheses attribute altered LGM moisture to a strengthening and meridional compression of the storm track (Oster et al., 2015a) or a primarily thermodynamic control arising from steepened temperature and moisture gradients from the Pacific inland due to the cooling influence of the Laurentide Ice Sheet (Boos, 2012; Löfverström and Liakka, 2016; Morrill et al., 2018). Other hypotheses call upon a strengthening of moisture transport to the W-US from a southwesterly, subtropical source (Lyle et al., 2012) perhaps due to increased contributions from atmospheric rivers (Lora et al., 2017; Lofverstrom, 2020) driven by a southward shift of the Intertropical Convergence Zone (ITCZ) and intensification of North Pacific Hadley circulation (McGee et al., 2018).

Debate also surrounds model-proxy comparison. Although the general pattern of W-US hydroclimate response at the LGM is robust, proxy records are not direct measures of hydroclimate, which can make model-proxy comparison difficult. For example, proxy-data archives that record amount weighted  $\delta^{18}O$  values of precipitation ( $\delta^{18}O_p$ ) may be influenced by changes in the  $\delta^{18}O$  values from different moisture sources, relative amount of precipitation from different moisture sources, rainout and infiltration of water vapor during transport, seasonality of precipitation, fractionation during condensation, and local below cloud processes (e.g., Pausata et al., 2011; Pausata and Löfverström, 2015; Tabor et al., 2018; He et al., 2021). In the case of  $\delta^{18}O$  of speleothem carbonate ( $\delta^{18}O_c$ ), changes in cave air temperature at the time of deposition, mixing of water sources, and evaporation in the soil and karst compound the complexity (e.g., Fairchild et al., 2006;

Tremaine et al., 2011; Baker et al., 2012). Therefore, attribution of  $\delta^{18}\text{O}$  variations to changes in temperature or precipitation is often overly simplified and potentially erroneous. Water isotopologue tracking enabled Earth system models have the potential to separate the various climate signals stored in isotopic records. By tracking the physical and dynamical movement of  $H_2^{18}\text{O}$  and  $H_2^{16}\text{O}$  within the Earth system, one can better determine what mechanisms and interactions are responsible for the  $\delta^{18}\text{O}$  signals found in the W-US at the LGM.

Studies typically utilize monthly climatologies of model outputs when informing proxy interpretations. However, exclusively exploring climatology can limit understanding about the specific weather patterns underlying past climate signals. For example, atmospheric rivers (ARs) are elongated plumes of concentrated water vapor that overall account for roughly 90% of the total meridional water vapor flux in the mid-latitudes but individually only last for hours to days (Zhu and Newell, 1998; Guan and Waliser, 2015). Recent work by Lora et al. (2017) and Lofverstrom (2020) suggests that ARs are largely responsible for the moisture increase in the southwest US at the LGM. Yet most studies are unable to distinguish the role of ARs in the W-US moisture budget due to working with monthly means, which cannot well separate the drivers of past hydroclimate change. Therefore, high temporal frequency outputs from models are required to better understand the mechanisms driving the proxy signals.

Here, we present preindustrial (PI; 1850 CE) and LGM Earth system model simulations that include online water isotopologue tracers. Our experiments include high temporal frequency data outputs. Together, these features allow for new insights into the drivers of W-US hydroclimate and isotopic change at the LGM. We subsequently use proxy forward models to compare our climate modeling results to speleothem  $\delta^{18}$ O records from the W-US. In section 2, we detail the earth system model, experiment configurations, and water tracking techniques that we use to determine mechanisms responsible for W-US hydroclimate and isotopic change at the LGM. In section 3, we present our results, including W-US changes between LGM and PI in climatology and dynamics as well as several sensitivity experiments with different combinations of LGM and PI boundary conditions. In section 4, we follow with a comparison between model simulations and speleothem  $\delta^{18}$ O records, made possible using two karst system proxy models. Finally, we summarize our findings in section 5.

#### 2. Methods

#### 2.1. Earth system modeling

Here, we use the Community Earth System Model version 1.3 with water isotopologue tracking of oxygen and hydrogen in the atmosphere, land, ocean, sea ice, and runoff components (iCESM1.3; Nusbaumer et al., 2017; He et al., 2021). The climate of CESM1.3 is broadly similar to CESM1.2, which accurately captures the observed PI and historical mean state and variability (Hurrell et al., 2013); the simulated present-day water isotopologues are also similar in both model versions (Brady et al., 2019). Moreover, iCESM1.3 demonstrates skill capturing the observed spatial pattern of  $\delta^{18}\mathrm{O}_p$  depletion moving inland from the US west coast (Fig. S1) and more generally when compared with proxy records from the LGM (e.g., Zhu et al., 2017; Tierney et al., 2020; He et al., 2021). CESM1 has also been used in paleo-atmospheric river research (Skinner et al., 2020; Shields et al., 2021).

This study explores changes in W-US hydroclimate between the Last Glacial Maximum (LGM; 21 ka) and preindustrial (PI; 1850 CE). To this end, we use four configurations of iCESM1.3 to simulate the two time periods of interest (Fig. S2). Our PI boundary conditions

come from the CESM1 default datasets for 1850 CE (Hurrell et al., 2013). Our LGM boundary conditions follow the Paleoclimate Modelling Intercomparison Protocol version 4 (PMIP4) for the LGM (Kageyama et al., 2017), including ICE-6G ice sheet reconstructions (Peltier et al., 2015), 21 ka orbital configuration (Laskar et al., 2011), and 190 ppm CO<sub>2</sub> (Bereiter et al., 2015). Initial isotopic distribution in the ocean comes from the GISS interpolated ocean  $\delta^{18}$ O dataset (LeGrande and Schmidt, 2006) with global enrichment of +1.05% in the LGM simulation to account for the increase in terrestrial ice (Duplessy et al., 2002). In addition to the full LGM forcing simulation, we perform two sensitivity tests. One sensitivity experiment, PI\_Topo, uses all LGM boundary conditions except topography, which is set to PI values. In other words, the PI\_Topo experiment includes LGM greenhouse gases, orbit, ocean conditions, land surface types, and land/sea mask with PI ice sheet elevation. The other sensitivity experiment, LGM\_Topo, uses all PI boundary conditions except topography, which is set to LGM values. In other words, the LGM\_Topo experiment includes PI greenhouse gases, orbit, ocean conditions, land surface types, and land/sea mask with LGM ice sheet elevation.

We initialize and spin-up the water isotopologues in the LGM and PI experiments using the fully coupled configuration of iCESM1.3 with  $1.9^{\circ} \times 2.5^{\circ}$  horizontal resolution atmosphere (Community Atmosphere Model 5; CAM5) and land (Community Land Model 4; CLM4) components, and nominal 1° horizontal resolution ocean (Parallel Ocean Program 2; POP2) and sea ice (Community Sea Ice Model 4; CICE4) components. We integrate these fully coupled simulations until the climates and distributions of water isotopologues are near equilibrium (long-term drift is small compared to interannual variability). We then switch to a  $0.9^{\circ} \times 1.25^{\circ}$  horizontal resolution configuration of iCESM1.3 with dynamically evolving atmosphere and land models (CAM5/CLM4only simulation) but prescribed monthly varying sea-surface conditions (temperature, sea-ice extent, and  $\delta^{18}$ O) from the last 50 years of the fully coupled simulations. The increased horizontal resolution allows the model to better resolve the topography that influences the climate in Western North America. To spin-up the land model (notably, soil temperatures and hydrology) at higher resolution, we first interpolate data from the  $1.9^{\circ} \times 2.5^{\circ}$  resolution simulations to the  $0.9^{\circ} \times 1.25^{\circ}$  grid, then run the CAM5/CLM4-only simulations for 50 years using an annual cycle of sea-surface conditions from the mean of the final 50 years of the fully coupled simulations. Next, we extend the CAM5/CLM4-only simulations for an additional 50 years with time varying sea-surface conditions from the final 50 years of the fully coupled simulations. All analyses presented here are based on the final 45 years of the simulations (the first 5 years are discarded as model spin up). Below we discuss results from the W-US (land area between 29°N and 49°N and 110°W-125°W). Further, we divide the W-US into the Southwest United States (SW-US: land area between 29°N and 39°N and 110°W-125°W) and the Northwest United States (NW-US; land area between 39°N and 49°N and 110°W-125°W; see white dashed lines in Fig. 1). This W-US region is considered for the bulk of our model analyses (sections 3.1-3.5). However, we discuss locations further east in sections 3.6, 4.2, and 4.3 due to a limited number of W-US speleothem records that cover the late glacial period.

We employ several analysis techniques to interpret hydrologic change in the W-US at the LGM. To better understand the sources and isotopic composition of moisture reaching the W-US, we utilize the water "tagging" feature within iCESM1.3, which tracks water and its isotopic composition from evaporation within user defined regions to deposition. Here, we focus on regions within the North Pacific, as this area is the source of most moisture transported to the W-US. This unique feature of iCESM1.3 has been previously utilized to understand paleoclimate variations in  $\delta^{18}\mathrm{O}_{\mathrm{p}}$  (e.g., Tabor et al.,

2018; He et al., 2021). We also use the TempestExtremes feature detection algorithm (Ullrich and Zarzycki, 2017; Ullrich et al., 2021) to track two specific weather event types that largely drive the climatological changes in W-US hydrology. We output 6-hourly (instantaneous) variables of integrated vapor transport (ITV), sea level pressure, surface winds, and 500 and 300 hPa geopotential height to track atmospheric rivers (ARs) and extratropical cyclones (ETCs) in the North Pacific. Previous studies using versions of CESM in combination with TempestExtremes show skill simulating and tracking ARs and ETCs when compared with observations (e.g., Zarzycki, 2018; Rhoades et al., 2020).

Parameters for AR identification include: 1) a minimum IVT threshold of 250 kg/m/s; 2) a minimum Laplacian of IVT of 50,000 kg/m/s/degrees<sup>2</sup>; 3) a minimum IVT area of 5 grid cells; 4) a radius of the discrete Laplacian of 20 grid cells; and 5) a minimum latitude of 15°N. These parameters create a similar pattern of North Pacific AR track density to previous work (Rhoades et al., 2020). ETCs are tracked by following local minima in the 6-hourly sea level pressure field. These minima must be at least 3 hPa lower than the background sea level pressure and storms with a positive geopotential thickness anomaly of at least 10 m between 300 and 500 hPa are excluded as warm core (i.e., tropical) cyclones. ETCs must last at least 60 h and travel at least 10° great circle distance such that stationary, climatological lows are not included. ETC counts from our iCESM1.3 PI simulation compare well with ETC counts produced using National Centers for Environmental Prediction Climate Forecast System Reanalysis data (Ullrich and Zarzycki, 2017).

#### 2.2. Model-proxy comparison

2.2.1. Western U.S. speleothem  $\delta^{18}$ O records drip water estimates

We compile W-US speleothem  $\delta^{18}$ O records from the literature, including those from the SISALv2 database (Oster et al., 2019; Comas-Bru et al., 2020) and other records that have been published following the most recent SISAL update (Oster et al., 2020, Fig. 2a). Three speleothem records from the W-US cover the LGM (21 ka): Cave of the Bells, Arizona (COB; Wagner et al., 2010), Fort Stanton Cave, New Mexico (FS; Asmerom et al., 2010), and Lake Shasta Caverns, California (LSC; Oster et al., 2020). An additional three speleothem records cover the late glacial period and are dated to within 2000 years of 21 ka: McLean's Cave, California (ML, maximum age ~19.4 ka; Oster et al., 2015b), Pinnacle Cave, Nevada of the Leviathan Chronology (LV, maximum age ~20 ka; Lachniet et al., 2014), and Cave Without a Name, Texas (CWN, maximum age ~19.3 ka; Feng et al., 2014). Of the speleothem records available for the W-US, only the Leviathan Chronology covers both the late glacial and the present. This lack of consistent coverage precludes us from computing anomalies in the speleothem  $\delta^{18}$ O records to compare with modeled LGM-PI  $\delta^{18}O_p$  anomalies. Instead, our approach focuses on estimating the absolute values of LGM drip water following the guidelines for model-proxy comparison using speleothem records described in Comas-Bru et al. (2019). We complement this approach by also evaluating proxy forward modeling techniques to estimate drip water and calcite  $\delta^{18}$ O using our climate model output.

Following Comas-Bru et al. (2019), we compute the mean and standard deviations for the three records covering the interval 21 ka +/- 500 years. For the three records that cover the late glacial but not 21 ka (ML, LV, CWN), we calculated the mean and standard deviation of the oldest 500 years of each record. We then compute the estimated "LGM" drip water  $\delta^{18}$ O for each cave location using these mean speleothem  $\delta^{18}$ O values and the mean annual surface temperature from the LGM model output of the model gridbox nearest to each cave's location. We use two different calcite-water

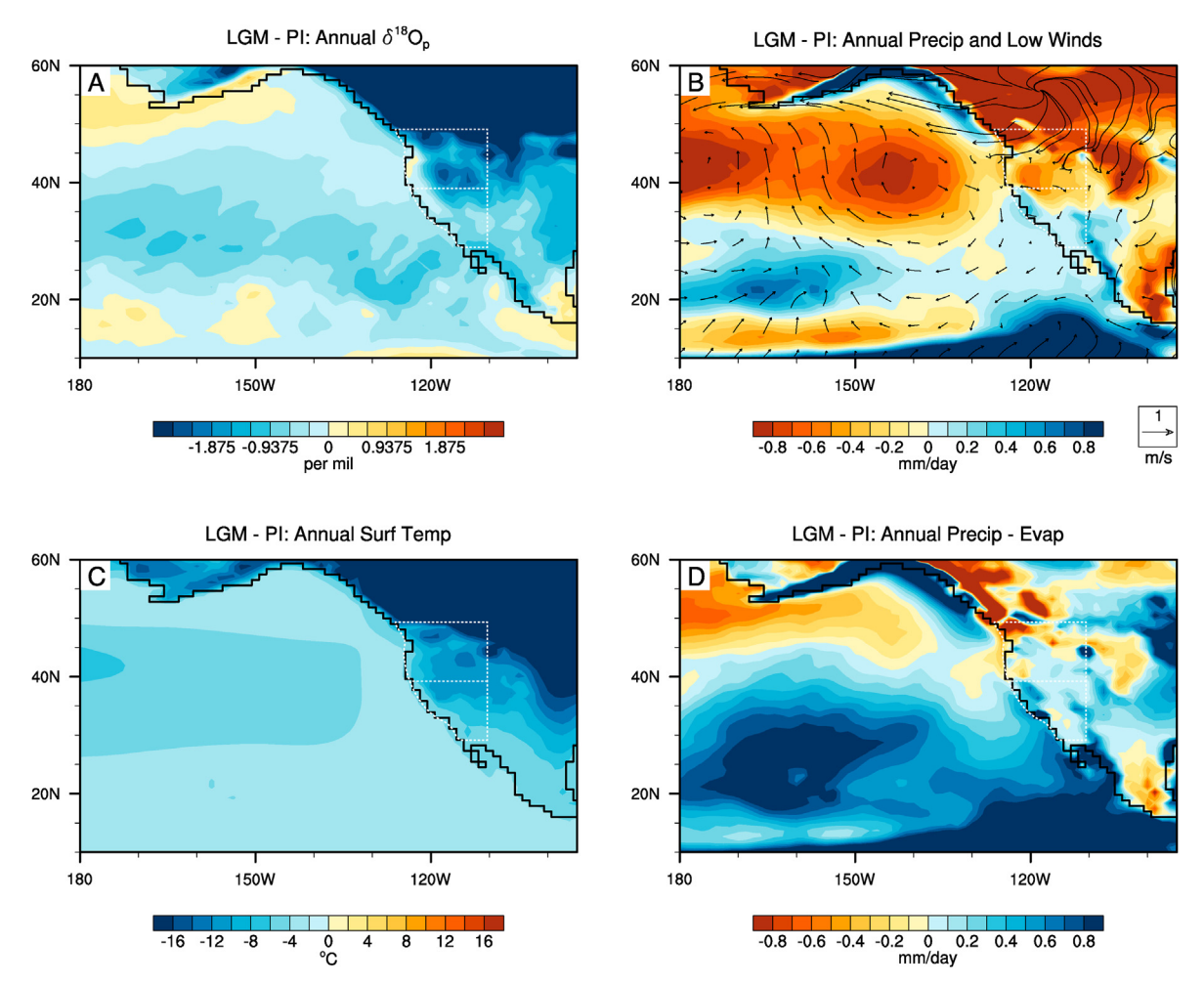


Fig. 1. Annual differences in climate between LGM and PI for A)  $\delta^{18}O_p$  of precipitation, B) precipitation and near surface winds, C) surface temperature, and D) precipitation minus evaporation. Northwest and Southwest United States regions outlined with dashed white lines. LGM continental configuration outlined in black.

oxygen isotope-fractionation relationships in our calculations: the experimentally determined low-temperature equilibrium fractionation relationship of Kim and O'Neil (1997) and the empirically determined, cave-specific water-calcite oxygen isotope fractionation relationship of Tremaine et al. (2011). We compare these estimated LGM drip water values to the amount-weighted  $\delta^{18}{\rm O}_p$  taken from the iCESM1.3 experiments mean annual and wettest consecutive three-month period for each cave location (Table S1).

## 2.2.2. Drip water forward modeling

To better understand the comparison between the iCESM1.3 experiments and the stalagmite records, we simulate stalagmite  $\delta^{18}\text{O}$  values using two different forward modeling approaches that have been developed for cave environments: CaveCalc and Karstolution. In this and following sections, we will distinguish between the iCESM1.3 experiments as described above in section 2.1 and the forward model experiments by referring to them as "CaveCalc runs" and "Karstolution runs", respectively. The first proxy system model, CaveCalc (Owen et al., 2018) forward models the evolution of carbonate fluid chemistry as water moves downward through the soil zone, the epikarst, and eventually into the cave. For CaveCalc, we input climatological (45-year mean) annual temperature and  $\delta^{18}\text{O}_p$  from the PI and LGM iCESM1.3 experiments for the grid cells in which each of our cave sites are located. For simplicity, we leave all other input parameters as their default values

following Owen et al. (2018), including a cave air  $p\text{CO}_2$  of 1000 ppm. CaveCalc does not allow for the diffusional exchange of soil gas with the atmosphere, so we do not account for differences in atmospheric  $p\text{CO}_2$  in these simulations. We run CaveCalc using the default multi\_step\_degassing Degassing/Precipitation Mode, which is meant to represent  $\text{CO}_2$  degassing and calcite precipitation during speleothem growth, and the default value of 0.5 as the fraction of  $\text{CO}_2$  removal per reaction step. During the model simulation, water undergoes progressive  $\text{CO}_2$  degassing and precipitates calcite (maintaining a saturation of 1.0) until the solution reaches equilibrium with the cave air. We consider the mean  $\delta^{18}\text{O}$  value of calcite precipitated over all the degassing steps as representative of the mean speleothem  $\delta^{18}\text{O}$  formed during the LGM and PI at each cave site.

In contrast to CaveCalc, which produces one value for the estimated speleothem  $\delta^{18}O$  for each of the LGM and PI time slices, Karstolution (Treble et al., 2019) uses a time series as an input and outputs a modeled time series of calcite  $\delta^{18}O$  that represent five different pseudo-stalagmites grown under conditions set by the user. Karstolution is a combination of KarstFor (Bradley et al., 2010; Baker and Bradley, 2010; Baker et al., 2014; Treble et al., 2013), which is a karst processes model, and ISOLUTION (Deininger et al., 2012), which is an isotope enabled fractionation model. Rather than the mean annual values of temperature and  $\delta^{18}O_p$  used for CaveCalc, Karstolution uses as input monthly time series of

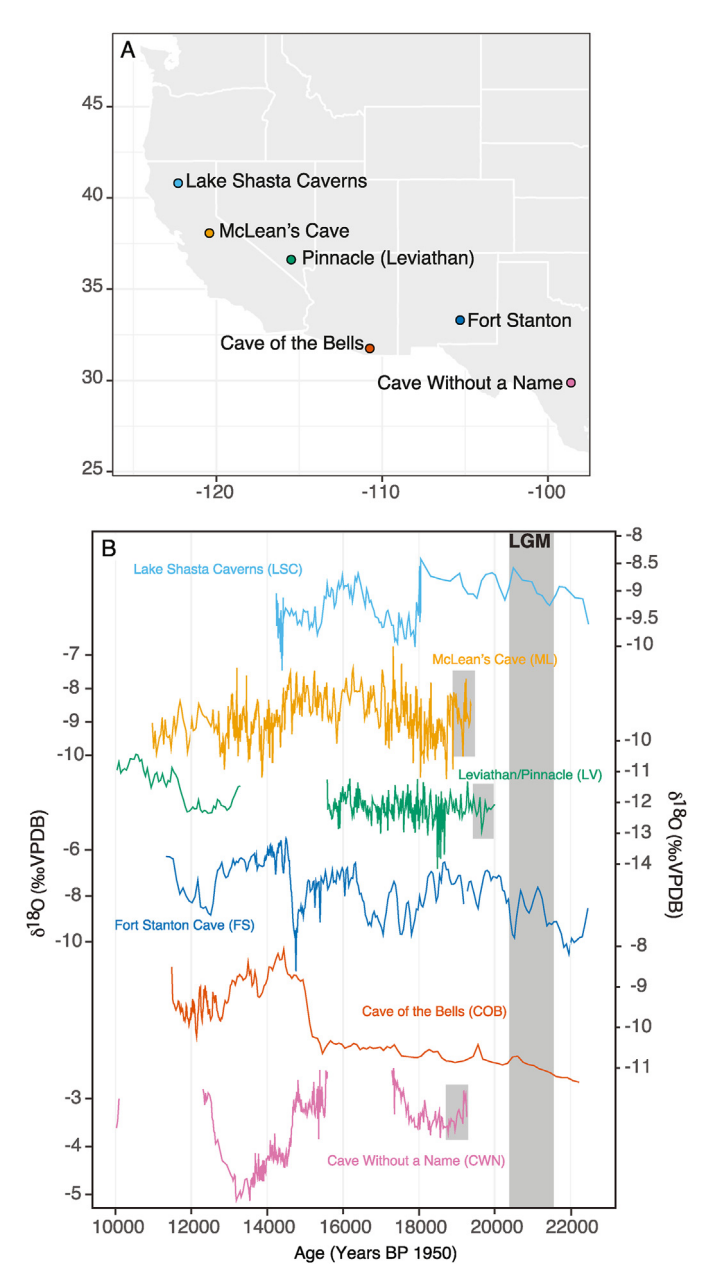


**Fig. 2.** W-US speleothem records with near LGM data. A) Map and B) time series of W-US speleothem  $\delta^{18}$ O records included in this study. Gray shading on B shows intervals of each record that are considered for the LGM comparisons with iCESM1.3. For records that extend to 21 ka, this includes 21 ka +/- 500 years. For records that do not extend to 21 ka, this includes the oldest 500 years of each record.

precipitation and evaporation amounts, temperature, and  $\delta^{18}O_p$  from the iCESM1.3 experiments. In addition, the model uses a configuration file, which prescribes the fluxes through the karst portion of the model, the cave-air  $pCO_2$ , the cave-air temperature, and the relative humidity. Coupling of KarstFor and ISOLUTION to develop Karstolution allows for a better understanding of the impacts of climatic karst processes and in-cave effects on calcite  $\delta^{18}O$ , as the model can be tuned based on information from cave monitoring to represent the karst processes understood for a given cave system.

To run Karstolution, we use 45 years of monthly outputs, as opposed to the mean annual values used in CaveCalc, from the PI and LGM iCESM1.3 experiments from the grid cells that include

each cave location. In these initial runs of Karstolution, cave-air  $p\text{CO}_2$  was set to the atmospheric  $p\text{CO}_2$  used for the iCESM1.3 experiments (190 ppm at LGM, 284.7 ppm at PI). The initial  $\delta^{18}\text{O}$  value of the karst storage water and cave-air temperature in the configuration file was set to the mean annual  $\delta^{18}\text{O}_p$  and temperature from the iCESM1.3 outputs for the cave location. The five hypothetical calcite  $\delta^{18}\text{O}$  time series produced by Karstolution capture different configurations of mixing between reservoirs of water in the karst and soil water (Treble et al., 2019). In this paper, we present the Karstolution results for Stalagmites 2 and 4 as these two simulated stalagmite time-series represent a short water-residence time endmember (Stalagmite 2) and a longer water-residence time endmember (Stalagmite 4) (Fig. S3).

We completed a set of Karstolution runs for each cave location using the same settings at each site. However, to further explore the influence of in-cave processes on the forward-model results, we made use of extensive cave monitoring data that have been published for the two California Cave sites, LSC and ML, allowing us to compare the iCESM1.3 output with pseudo-stalagmites tuned with site-specific information. The relevant monitoring data that exist for these sites include seasonal measurements of cave air pCO<sub>2</sub> and relative humidity at LSC (Oster et al., 2020) and Black Chasm Cave, which is close to ML (Oster et al., 2012). A second set of Karstolution runs were carried out for these two sites using cave monitoring data and site-specific parameterization of cave seasonality and are referred to as "optimized" Karstolution runs. Based on these monitoring data, for ML we prescribed a cave-air pCO<sub>2</sub> of 1000 ppm for the year except for the Boreal summer (JJA), which was prescribed at 3000 ppm. The relative humidity was set at 95% and the cave-air temperature was set to the mean annual from the iCESM1.3 experiments. For ML, the temperature used is -2.2 °C with a 4 °C temperature increase for JJA. For LSC, we prescribed a cave-air pCO<sub>2</sub> of 470 ppm. The relative humidity was set to 89% for JJA and 95% for the rest of the seasons. The cave-air temperature was set to the mean annual from the iCESM1.3 experiments for the LSC location (2.3 °C) with a 5 °C temperature increase for JJA.

#### 3. Results

#### 3.1. Climatology

As a spatial average, mean annual  $\delta^{18}O_p$  decreases by 1.33‰ in the W-US at the LGM compared to PI, with the greatest reduction in the north-central to north-east portion of the study area, and minimal change along the west coast (Fig. 1; Fig. S4). Similarly, the SW-US and NW-US regions show reductions in mean annual  $\delta^{18}O_p$  at the LGM of 0.79‰ and 1.70‰, respectively. There exist some similarities in the spatial patterns of changes in mean annual surface temperature, precipitation, and  $\delta^{18}O_p$  in the W-US at the LGM. For example, regions of lower  $\delta^{18}O_p$  are generally associated with areas of drying and enhanced surface cooling. However, these spatial relationships are the product of several changes in LGM climate, and local temperature and precipitation cannot be considered causative of the  $\delta^{18}O_p$  response.

Like the spatial pattern of precipitation observed in previous modeling and proxy data studies (e.g., COHMAP Members, 1998; Bartlein et al., 2011; Oster et al., 2015a; Morrill et al., 2018), in our simulations the SW-US experiences a small mean annual increase in precipitation of 11.4 mm/year, while the NW-US experiences a pronounced mean annual decrease in precipitation of 171.7 mm/year at the LGM relative to PI (Fig. 1; Fig. S4). A decrease in evaporation associated with cooler surface temperatures at the LGM further moistens the SW-US and results in a variable net moisture response in the NW-US despite the pervasive reduction in precipitation.

Because this study focuses on the mechanisms driving W-US changes in  $\delta^{18}O_p$  at the LGM, precipitation amount is a primary interest. In the W-US, 61% and 58% of mean annual precipitation falls in the cool season (here defined as November to March) in the LGM and PI simulations, respectively (Fig. S5), due primarily to extratropical cyclones. Although the cool season contribution to mean annual precipitation decreases moving inland, much of the remaining W-US precipitation occurs during the fall and early spring and is also due primarily to extratropical cyclones. Cool season hydroclimate, therefore, well reflects the mechanisms driving the annual  $\delta^{18}O_p$  response in this region and will be the focus of the following model results. Note, we do not limit our analyses to cool season precipitation when comparing with speleothem  $\delta^{18}O$  in section 3.6.

As expected, the W-US mean annual  $\delta^{18}O_p$  response generally reflects the W-US cool season  $\delta^{18}O_p$  response between LGM and PI, especially along the North American west coast where the cool season contribution to annual precipitation is greatest (Fig. 3; Fig. S6). Only the small area more positive cool season  $\delta^{18}O_p$  in the south-central sector of the study region disagrees in sign with the mean annual response (see further discussion below). During winter, there is anomalous low-level onshore flow in the SW-US and offshore flow in the NW-US, which generally aligns with areas of more and less cool season and annual precipitation. The cool season surface temperature anomaly also agrees with the

mean annual response, depicting rapid cooling towards the continental interior. Notably, the spatial pattern of W-US cool season  $\delta^{18} O_p$  response at the LGM does not correlate with changes in precipitation amount.

#### 3.2. Water tagging

To better understand the simulated LGM  $\delta^{18}O_p$  response, we track moisture that sources from different regions of the North Pacific. The results show that changes in both the cool season  $\delta^{18}O_{\rm p}$ and precipitation in the Central East North Pacific region (CENP; here defined as the region 20°N-45°N, 180°W-US coast) contribute most significantly to the LGM  $\delta^{18}O_p$  response in the W-US (Fig. 4; Fig. S7). First,  $\delta^{18}O_p$  and  $\delta^{18}O$  of water vapor ( $\delta^{18}O_{wv}$ ) in the W-US from the CENP region are relatively lower at the LGM than the PI. The similarity of  $\delta^{18}O_{\rm p}$  and  $\delta^{18}O_{\rm wv}$  changes from the CENP region signify that the W-US reduction in  $\delta^{18}O_p$  at the LGM is largely a result of differences in the isotopic composition of the water vapor. The change of  $\delta^{18}O_{WV}$  is small in the eastern North Pacific, which indicates evaporative conditions, likely related to cooling, offset the ~1% higher mean ocean  $\delta^{18}$ O at the LGM. The reduction of  $\delta^{18}$ O<sub>wv</sub> increases substantially moving inland, suggesting that rainout drives the lowering of  $\delta^{18}O$  from the CENP region into the continental interior. Moreover, the similar responses of  $\delta^{18}O_{wv}$  and  $\delta^{18}O_{p}$ in the W-US from the CENP region suggest minimal contributions

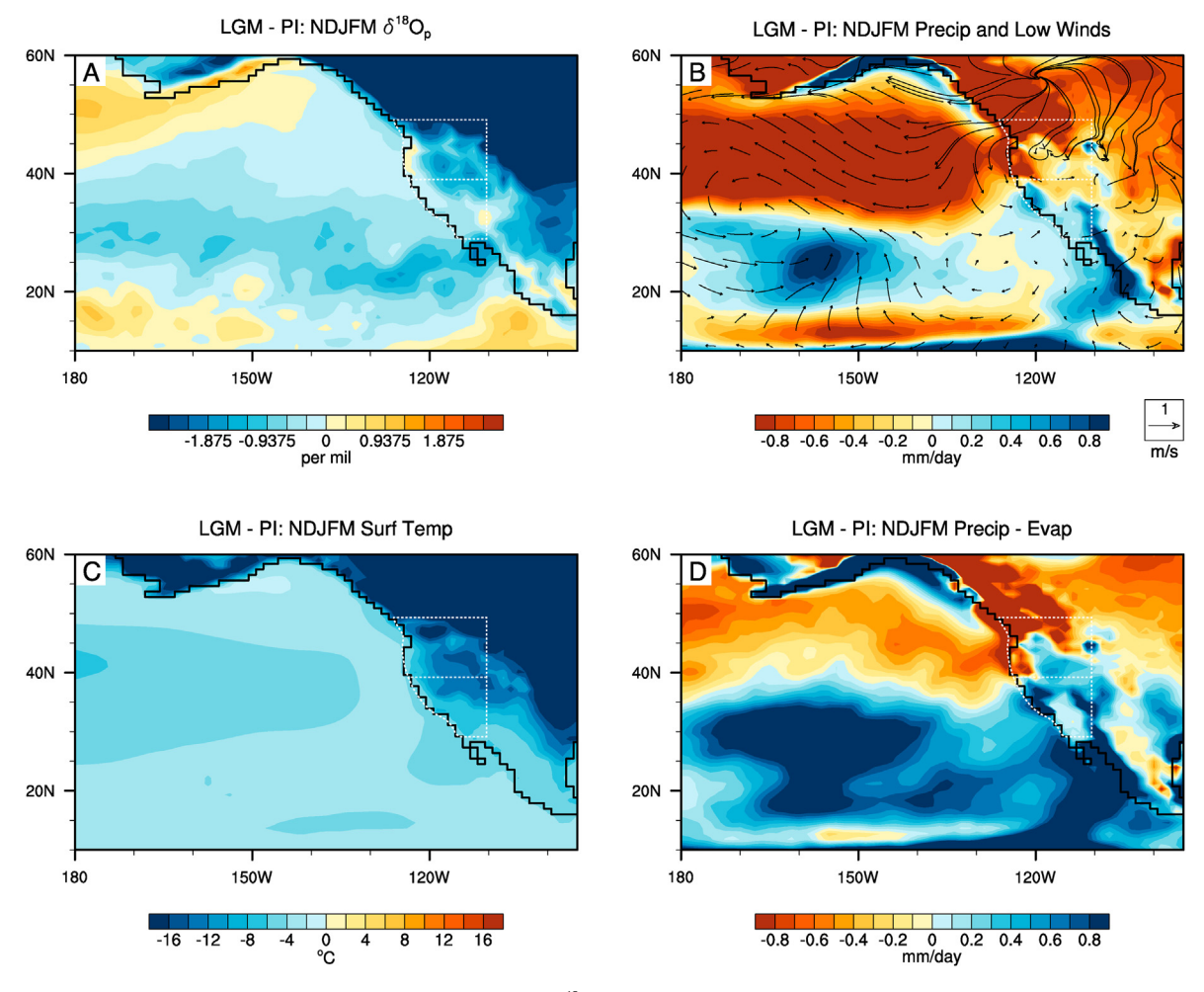


Fig. 3. Cool season (Nov-Mar) differences in climate between LGM and PI for A)  $\delta^{18}O_p$  of precipitation, B) precipitation and near surface winds, C) surface temperature, and D) precipitation minus evaporation. Northwest and Southwest United States regions outlined with dashed white lines. LGM continental configuration outlined in black.

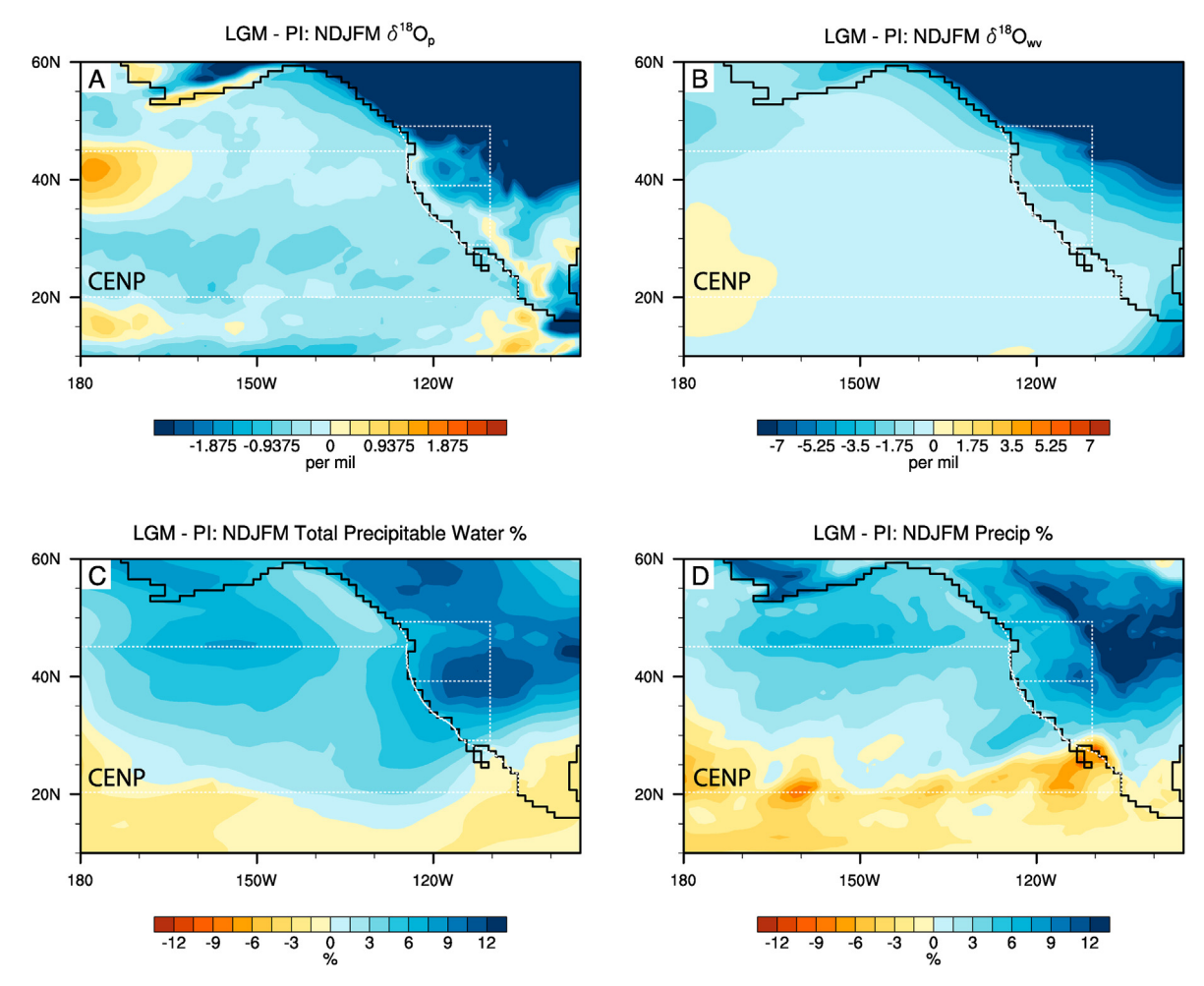


Fig. 4. Cool season (Nov–Mar) differences in climate from the water tagged Central North Pacific (CENP;  $20^{\circ}$ N- $45^{\circ}$ N,  $180^{\circ}$ W-US coast) region between LGM and PI for A)  $\delta^{18}$ O<sub>p</sub> of precipitation, B)  $\delta^{18}$ O<sub>wv</sub> of water vapor, C) percentage change in contribution to total precipitable water, and D) percentage change in contribution to total precipitation. Northwest and Southwest United States regions and Central North Pacific (CENP) tagged region outlined with dashed white lines. LGM continental configuration outlined in black.

from changing local fractionation to the overall  $\delta^{18}O_p$  response. Second, in addition to producing about half of the total cool season precipitation in the W-US, the CENP region contributes relatively more of the total precipitation to the W-US during the LGM than during the PI at the expense of precipitation sourced from farther west and north as well as reduced recycling over land. Reduction in precipitation from these more distant sources that provide relatively depleted moisture to the W-US limits the overall depletion in  $\delta^{18}O_{\rm p}$  at the LGM, particularly along the west coast. However, the 5-10% increase in W-US precipitation from the CENP region means the lower  $\delta^{18} O_{\text{p}}$  from this region has greater weight in the mean annual  $\delta^{18} O_p$  decrease at the LGM. The relative increase in W-US precipitation from the CENP region at the LGM mirrors an increase in W-US precipitable water from the CENP region, suggesting that changes in moisture transport from the CENP region plays an important role in cool season precipitation response.

## 3.3. Tempestology

We further explore the changes in moisture transport by tracking simulated cool season extratropical cyclones (ETCs) and atmospheric rivers (ARs). The relative increase in cool season CENP moisture reflects an increase and southward shift in North Pacific ETC activity during the LGM (Fig. 5; Fig. S8). Greater cool season cyclogenesis in the North Pacific appears related to locations of

increased baroclinicity associated with stronger latitudinal temperature gradients (Kageyama et al., 2017; Routson et al., 2019); LGM topography also likely plays a role (see further discussion in section 3.5). Despite a general increase in ETC activity in the Northeast Pacific between 25° and 55°N, there is a decrease in total moisture export from this region. However, moisture transport remains unexpectedly high relative to the decrease in precipitable water near the southwest coast, likely due to an intensification and southward shift of the low-level jet associated with greater ETC activity (Laîné et al., 2009; Wang et al., 2018). Likewise, AR frequency near the southwest coast shows only a small reduction at the LGM relative to PI. The cool season AR response at the LGM relates to the cool season ETC response as ARs are almost always associated with ETCs (Guo et al., 2020). Note, our use of AR thresholds chosen for present-day societal impacts might be partly responsible for the discrepancy in response between ETCs and ARs (see further discussion in section 4.1). Given the dramatic cooling and overall decrease in precipitable water at the LGM, the similar amount of cool season moisture transport into the SW-US between time periods is noteworthy. However, there is an increase in precipitation throughout the SW-US region at the LGM, suggesting that maintenance of Pacific cool season moisture transport is not the only mechanism driving the SW-US hydroclimate response.

In the NW-US, cooler temperatures, and associated reduction in humidity, in combination with a weaker low-level jet lead to a large

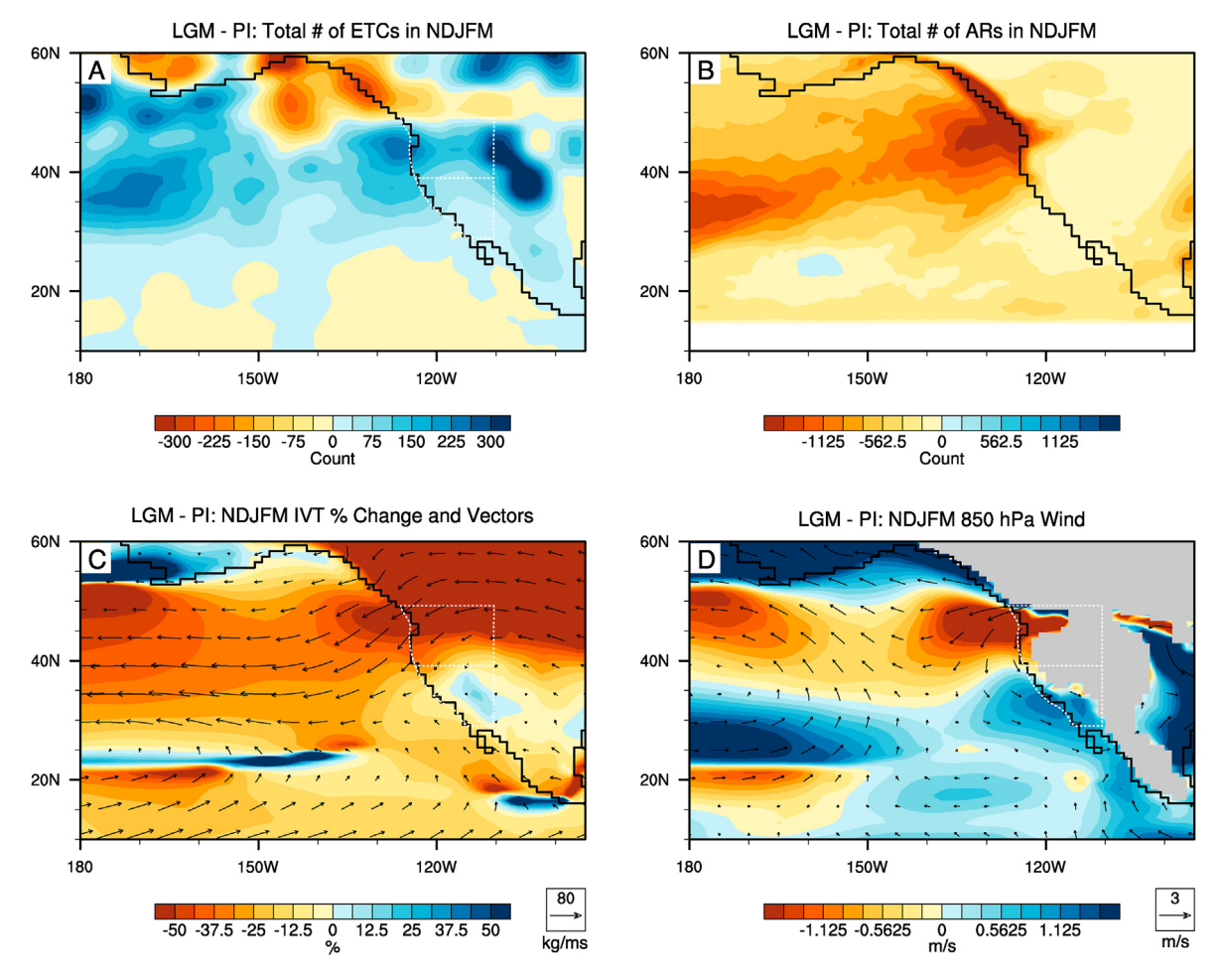


Fig. 5. Cool season (Nov—Mar) differences in storm activity between LGM and PI for A) total number of marine forming extratropical cyclones over 45 years of simulation using 6 hourly data and a 6 grid cell (-6°) search radius, B) total number of atmospheric rivers over 45 years of simulation using 6 hourly identifications, C) percent change in integrated vapor transport, and D) 850 hPa winds. Northwest and Southwest United States regions outlined with dashed white lines. LGM continental configuration outlined in black.

decrease in moisture transport at the LGM. In addition, the southward shift in the location of cool season ETCs near the west coast at the LGM modifies the location of offshore and onshore flow such that the warm sector impacts further south. Together, these changes help to reduce precipitation in the NW-US at the LGM.

#### 3.4. Efficiency and seasonality

The  $\delta^{18}O_p$  and precipitation responses in the W-US at the LGM are also due to greater moisture removal efficiency, defined here as the amount of precipitation in a region relative to the amount of column integrated water vapor in the same region. At the LGM, enhanced land-sea thermal contrast results in steeper slopes of the density surfaces, a rapid reduction in saturation vapor presssure, and greater condensation moving inland (Fig. 6; Fig. 3; Fig. S9), which produce more moisture convergence as the cool season storm systems move east despite reduced total precipitable water relative to PI. Enhanced storminess and more upslope flow along topography on the west coast of the US may also contribute to the greater cool season moisture removal efficiency at the LGM. In general, greater moisture removal efficiency leads to enhanced depletion inland due to the preferential removal of the heavier isotopes near the coast. Higher coastal  $\delta^{18}O_{wv}$ , which results from increased moisture flux from the nearby ocean and the increase in mean seawater  $\delta^{18}$ O at the LGM, quickly transitions to lower  $\delta^{18}$ O<sub>wv</sub> farther inland because of increased rainout from stronger uplift and

cooling. This enhanced moisture removal efficiency is largely responsible for the cool season reduction in  $\delta^{18} O_{wv}$  and  $\delta^{18} O_p$  as moisture is transported into the continental interior at the LGM. Even with greater moisture removal efficiency, NW-US precipitation is reduced due to the large decrease in total moisture transport. The cold, dry air flowing down the LGM ice sheets further suppresses precipitation along the southern ice edge.

Because  $\delta^{18}O_p$  is a weighted quantity, changes in precipitation seasonality can also contribute to  $\delta^{18}O_p$ . Cool season  $\delta^{18}O_p$  is generally lower than other seasons in both the LGM and PI simulations (Fig. 7). The SW most portion of the W-US is an exception to this in the LGM simulation. Here, there is an increase in  $\delta^{18}O_p$ during the winter relative to summer likely due to more near coast moisture in the cold season. Because of the generally lower  $\delta^{18}O_p$  in the cool season, more precipitation in the cool season relative to the summer drives the mean annual  $\delta^{18}O_p$  signal towards lower values in the W-US. Indeed, cool season precipitation increases relative to annual precipitation in much of the W-US at the LGM. This seasonal shift is both a result of increased cool season precipitation associated with greater ETC activity and moisture removal efficiency, as well as decreased spring/summer precipitation associated with reduced convection in the LGM climate, possibly due to entrainment of cool, dry air from further north (Bhattacharya et al., 2017). The increase in cool season precipitation at the LGM is most pronounced in the Great Basin region, where cool season precipitation increases by ~15% with a clear response in mean annual  $\delta^{18}O_{\rm p}$ 

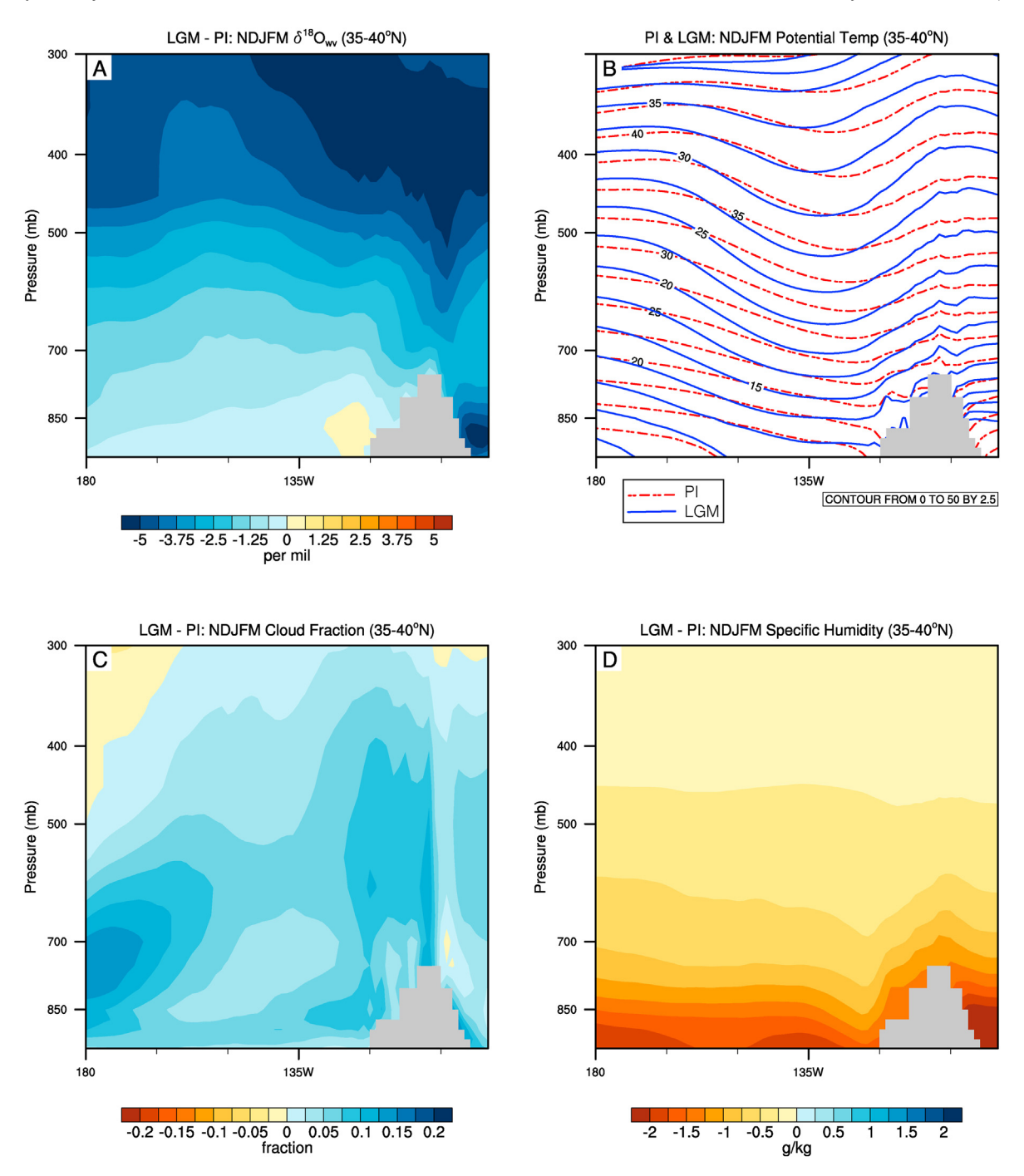


Fig. 6. Cool season (Nov—Mar) differences in climate between LGM and Pl as a vertical cross section from 35° to  $40^{\circ}$ N for A)  $\delta^{18}O_{wv}$  of water vapor, B) LGM and Pl lines of constant potential temperature (isentropes), C) cloud fraction, and D) specific humidity. LGM topography is shaded gray.

(Fig. 7; Fig. 1). Outside of this region, however, there are a few areas where seasonal changes in precipitation lead to a small increase  $\delta^{18}O_p$  at the LGM. In most of the W-US, areas of higher  $\delta^{18}O_p$  caused by changes in precipitation seasonality are offset by lower isotopic values of precipitation, which are largely a result of increased moisture removal efficiency at the LGM.

#### 3.5. Sensitivity experiments

Sensitivity experiments using either PI boundary conditions with LGM topography (LGM\_Topo) or LGM boundary conditions

with PI topography (PI\_Topo; see Section 2.1 for additional details) show that the W-US responses at the LGM are not the result of a single forcing. Neither sensitivity simulation produces as much mean annual reduction in  $\delta^{18}O_p$  in the W-US as the full forcing LGM simulation (Fig. 8), suggesting contributions from both dynamic and thermodynamic processes. That said, the large-scale North Pacific circulation anomaly at the LGM results primarily from sea surface temperature (SST) and albedo responses as seen in LGM\_topo while the west coast precipitation increase results primarily from topographic changes as seen in PI\_Topo. The overall SW-US precipitation response at the LGM appears to be a

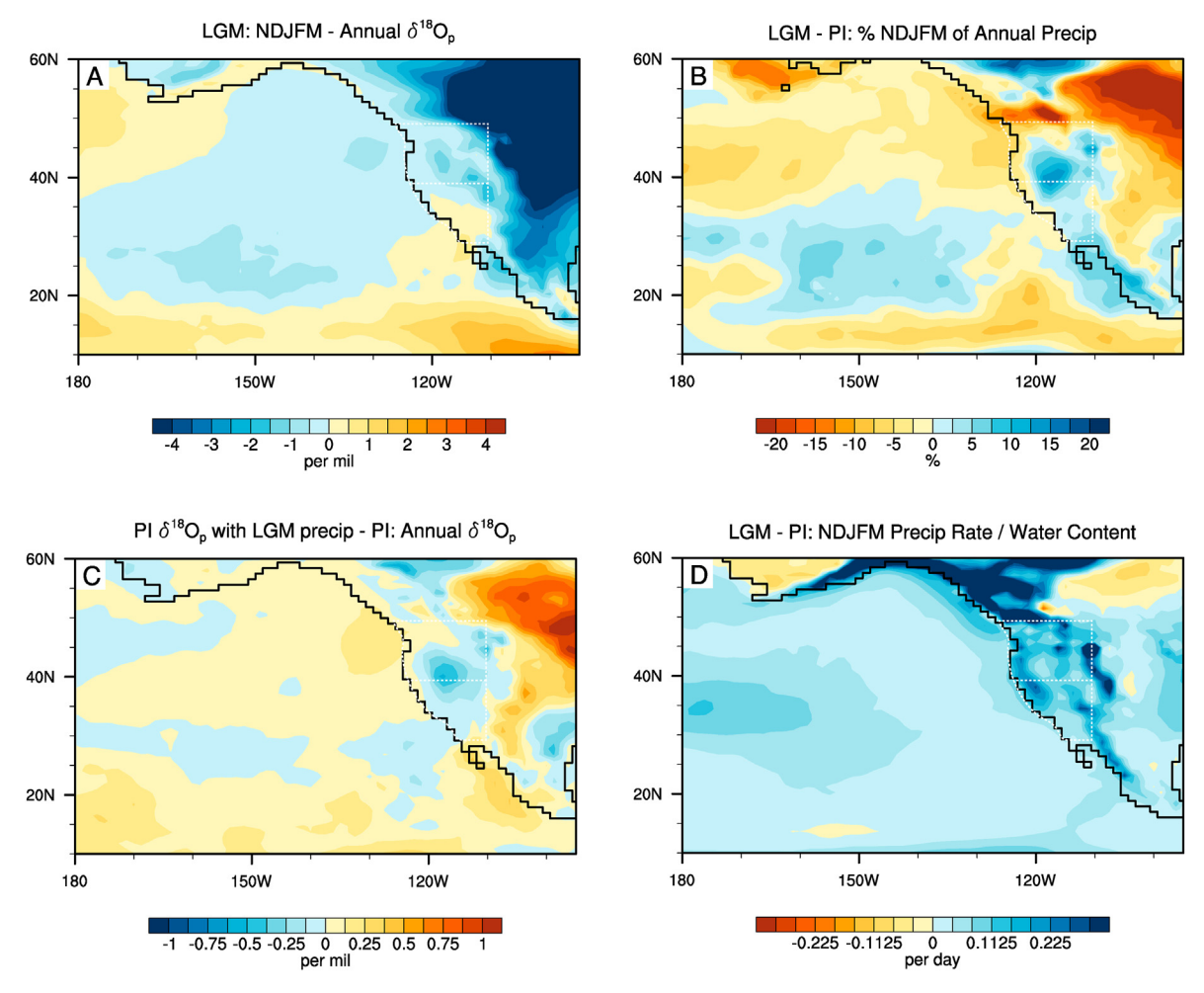


Fig. 7. Differences in seasonality for A) LGM  $\delta^{18}O_p$  of precipitation between cool season (Nov—Mar) and annual, B) changes in percent contribution of cool season precipitation to annual precipitation between LGM and PI, C) the impact of LGM precipitation seasonality on PI  $\delta^{18}O_p$  (i.e. comparing  $\delta^{18}O_p$  calculated using LGM precipitation and PI  $\delta^{18}O_p$  against  $\delta^{18}O_p$  calculated using PI precipitation and PI  $\delta^{18}O_p$ , and D) changes in cool season precipitation rate relative to total precipitable water between LGM and PI. Northwest and Southwest United States regions outlined with dashed white lines. LGM continental configuration outlined in black.

combination of LGM\_Topo and PI\_Topo forcings. In contrast, the general reduction in precipitation found in the NW-US region at the LGM is not a clear combination of topographic and SST changes. The lack of topographic barrier and dry downslope flow from the high pressure over the North American ice sheets allows for more onshore flow in PI\_Topo, resulting in an increase in cool season precipitation. Likewise, there is an increase in NW-US coastal precipitation in LGM\_Topo related to the increase in storm frequency (Fig. 9); however, outflow from the North American ice sheets dampens this response at the northern edge of the NW-US. In the full forcing LGM experiment, flow off the ice sheets in combination with cooler surface temperatures suppress the mechanisms driving increased NW-US coastal precipitation in PI\_topo and LGM\_topo. Even though both sensitivity experiments show increased and shifted cool season ETC activity in the North Pacific, only the LGM\_Topo experiment results in an associated increase in moisture transport by ARs, suggesting that the cooling at the LGM plays a large role in limiting the amount of moisture and precipitation in the W-US. There is also a large difference in the strength of the North Pacific low-level jet between simulations, with a pronounced southward shift in LGM\_topo like in the full forcing experiment. This dramatic change in jet strength clearly plays a role in vapor transport into the W-US, but the exact mechanisms for this response are beyond the scope of this study. These sensitivity

experiments also confirm that intensified land-ocean thermal gradients enhance cool season moisture removal efficiency in the W-US at the LGM as the PI\_Topo experiment shows an increase in coastal moisture removal efficiency. There is also enhanced moisture removal efficiency in the W-US in the LGM\_Topo experiment because of increased storm frequency and surface cooling on land due to the inclusion of LGM topography. Like in the full forcing LGM experiment, enhanced rainout of moisture moving inland leads to depletion of  $\delta^{18}O_p$  in these idealized cases, quickly offsetting potential enrichment due to increased moisture from nearby sources and mean ocean  $\delta^{18}O$  at the LGM. Seasonal changes in precipitation also likely contribute to the lower  $\delta^{18}O_p$  in these idealized runs relative to PI, especially in LGM\_Topo where storm activity significantly increases cool season precipitation. However, future work is needed to test these effects with fully interactive ocean and sea ice models.

#### 3.6. Proxy model comparison

A comparison of estimated LGM drip water  $\delta^{18}O$  values with modeled mean annual and wet season mean LGM  $\delta^{18}O_p$  is presented in Fig. 10a. Here, we define wet season precipitation as the three consecutive months that contribute most to annual rainfall at a particular location and time (Table S1). Thus, the wet season

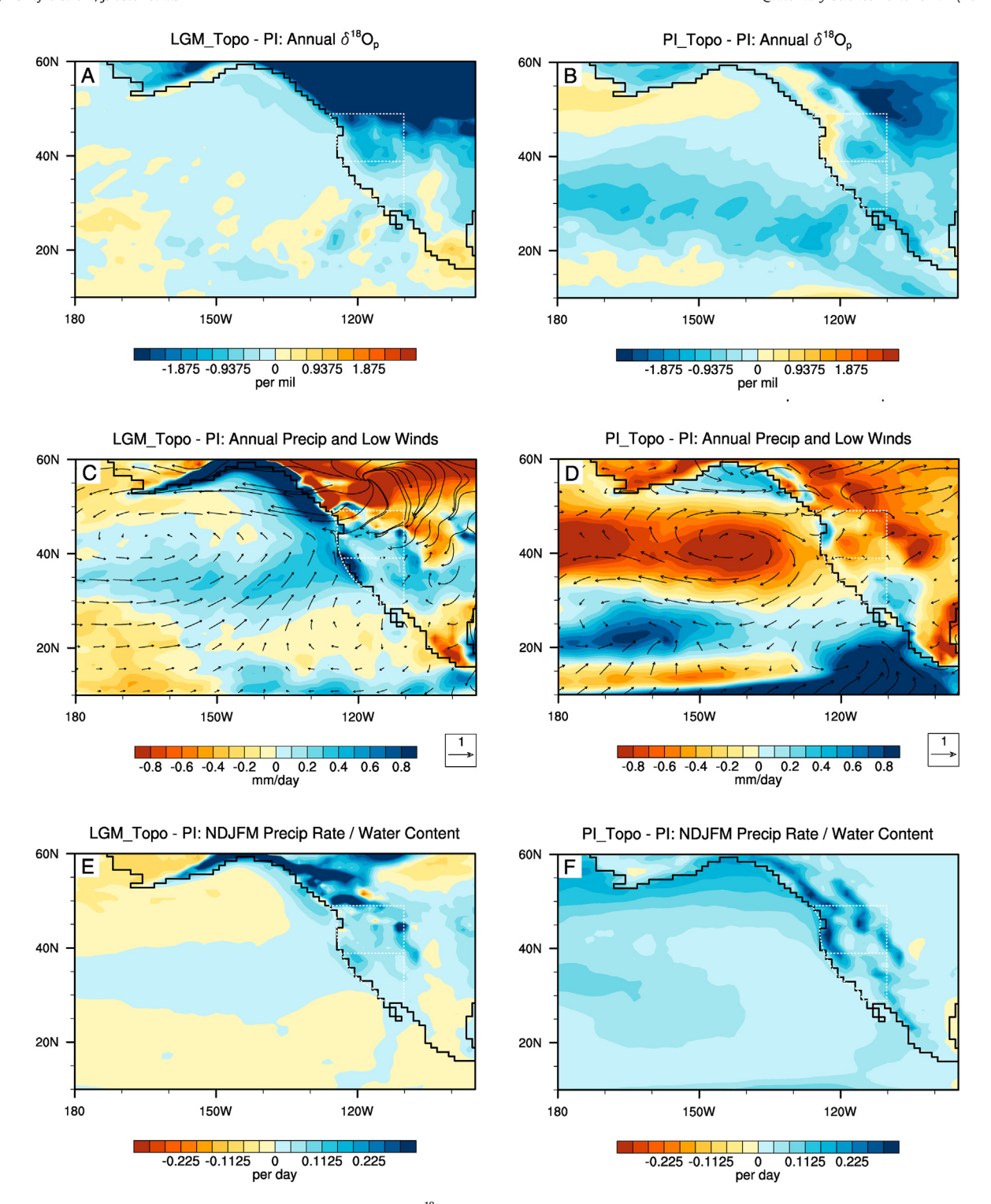


**Fig. 8.** Differences between sensitivity tests and PI. Differences in annual  $\delta^{18}$ O<sub>p</sub> of precipitation between A) LGM\_Topo and PI and B) Pl\_Topo and PI; cool season (Nov—Mar) precipitation and near surface winds between C) LGM\_Topo and PI and D) Pl\_Topo and PI; cool season precipitation rate relative to total precipitable water between I) LGM\_Topo and PI and J) Pl\_Topo and PI.

differs from site to site in this comparison. Estimated drip water  $\delta^{18}\text{O}$  values calculated using the Tremaine et al. (2011) empirical temperature-fractionation relationship are ~0.5–1% lower than values calculated using the Kim and O'Neil (1997) fractionation relationship. For many of the sites, one or both drip water estimates are within 0.5% of the modeled  $\delta^{18}\text{O}_{\text{p}}$ . At our most western sites, LSC and ML, drip water estimated using the Kim and O'Neil

relationship is more closely aligned with modeled  $\delta^{18}O_p$ , which is similar between the mean annual and wet season (DJF at these sites). At LV, both fractionation relationships produce estimated drip water that is within 0.5‰ of the mean annual  $\delta^{18}O_p$  from the model, while the wet season (DJF)  $\delta^{18}O_p$  value is almost 2‰ more negative than the estimated LGM drip water values. At FS, the Tremaine et al. (2011) fractionation relationship produces an

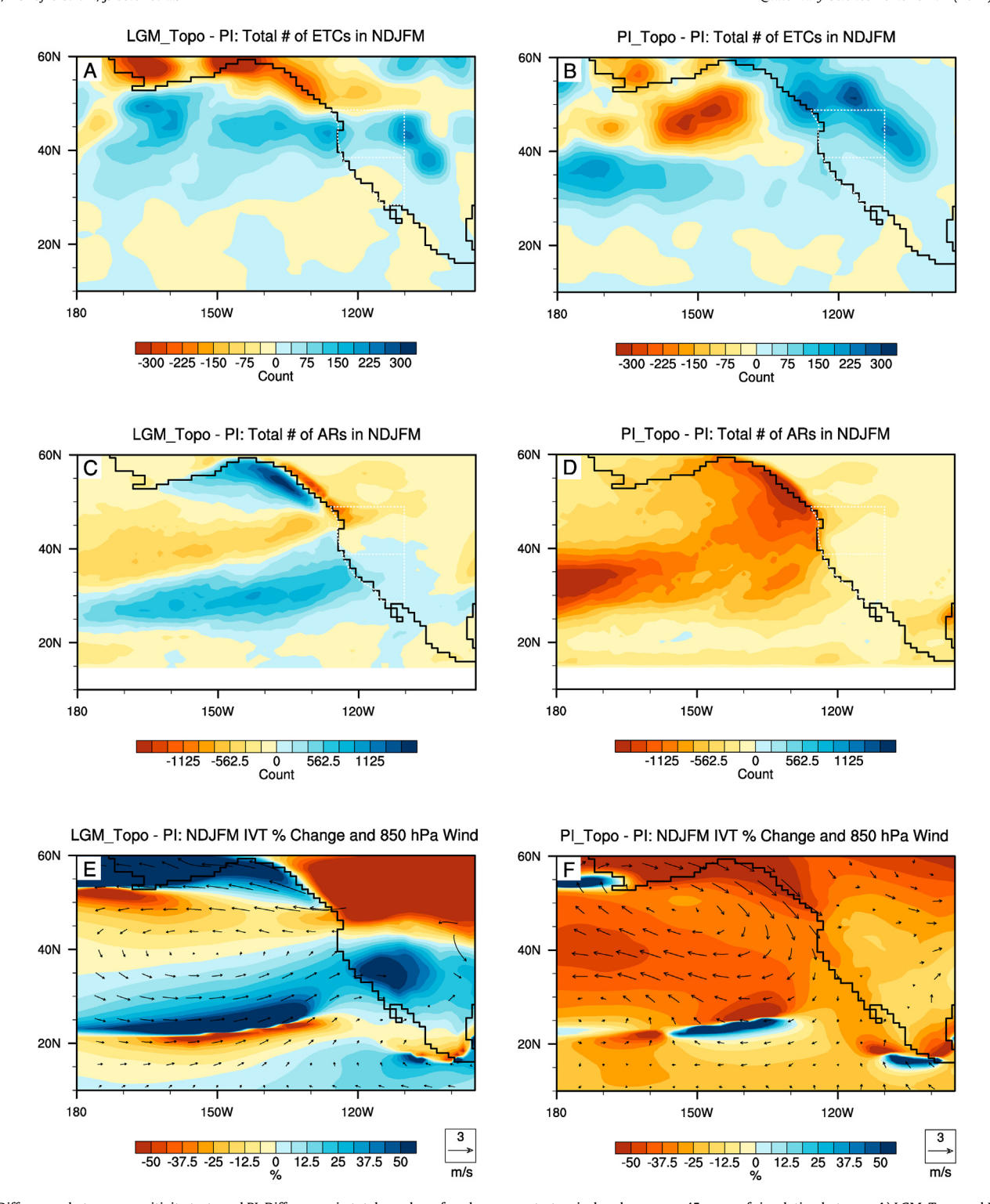


**Fig. 9.** Differences between sensitivity tests and Pl. Differences in total number of cool season extratropical cyclones over 45 years of simulation between A) LGM\_Topo and Pl and B) Pl\_Topo and Pl; total number of cool season of atmospheric rivers over 45 years of simulation between C) LGM\_Topo and Pl and D) Pl\_Topo and Pl; cool season percent change in integrated vapor transport and 850 hPa wind vectors between E) LGM\_Topo and Pl and F) Pl\_Topo and Pl.

estimated drip water value that is within ~1‰ of the model mean annual  $\delta^{18}O_p$  value, whereas the wet season (JJA) mean is much more negative than the estimated drip water. At COB, the Kim and O'Neil (1997) relationship produces estimated drip water that is very close (within ~0.5‰) of the modeled mean annual  $\delta^{18}O_p$ , with the wet season (JFM) values being more positive than the estimated drip water. The Texas site, CWN, displays the largest discrepancy

between drip water estimated from speleothem  $\delta^{18}O$  values and modeled  $\delta^{18}O_p$ , as the estimates of drip water (using both fractionation relationships) are several per mil more positive than the modeled precipitation.

A comparison of the forward proxy model results, Karstolution and CaveCalc, and the measured stalagmite  $\delta^{18}$ O from each cave site is presented in Fig. 10b. Karstolution runs result in a time series of

output (Fig. S3). For the purposes of comparison with CaveCalc and the speleothem values, we averaged the Karstolution time series and calculated the  $1\sigma$  (standard deviation) of the mean. For Karstolution, we focus on the speleothem  $\delta^{18}O$  estimates for Stalagmite 2 (short residence time) and Stalagmite 4 (long residence time). Stalagmite 2 displays more variability in the  $\delta^{18}$ O time series than Stalagmite 4 (Fig. S3) reflecting the short fluid residence time and thus has a larger standard deviation about the mean. Both the Karstolution Stalagmite 4, and the  $\delta^{18}$ O estimate from CaveCalc fall within the standard deviation of the mean  $\delta^{18}$ O of Stalagmite 2, indicating good agreement between the two forward proxy models used in this study for all cave sites, except COB. Further, the  $\delta^{18}$ O estimate from CaveCalc agrees within the standard deviation of the mean  $\delta^{18}$ O of the less variable Stalagmite 4 for all sites except COB. The CaveCalc estimate for COB is ~0.8% lower than the estimate for Stalagmite 4.

The CaveCalc and Karstolution estimates of  $\delta^{18}O$  agree well with the measured speleothem  $\delta^{18}O$  for many of the sites. However, the measured stalagmite  $\delta^{18}O$  at CWN is ~5% higher than the estimates from the proxy model runs, and stalagmite  $\delta^{18}O$  at LSC is ~1% lower than the proxy model results. A comparison of the fully optimized Karstolution runs and the measured stalagmite  $\delta^{18}O$  for cave sites LSC and ML is presented in Fig. 10c. The optimized output for Stalagmite 2 agrees with the measured speleothem  $\delta^{18}O$  for LSC and ML. Additionally, the mean of the Stalagmite 4  $\delta^{18}O$  values agrees with measured  $\delta^{18}O$  values in the ML stalagmite and is within 0.5% of the measured LSC speleothem  $\delta^{18}O$  value. Thus, the proxy forward model results replicate well the measured stalagmite  $\delta^{18}O$  values for the LGM from these six cave sites except for CWN, and the inclusion of cave monitoring results in the forward modeling process improves these comparisons.

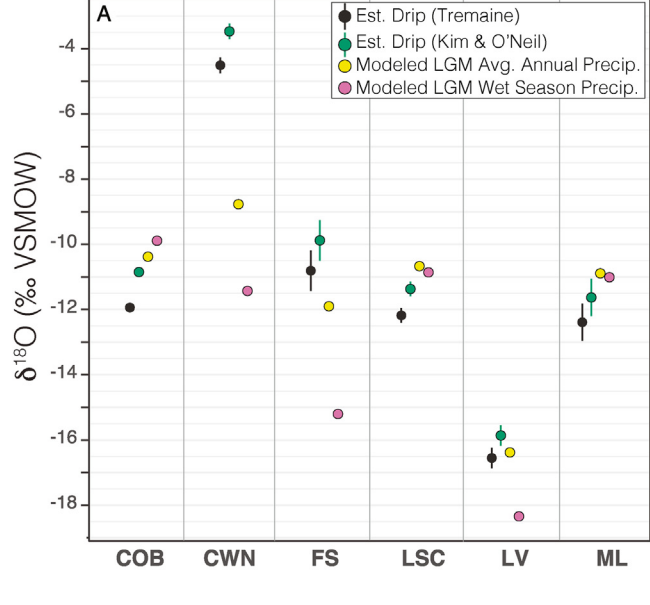
#### 4. Discussion

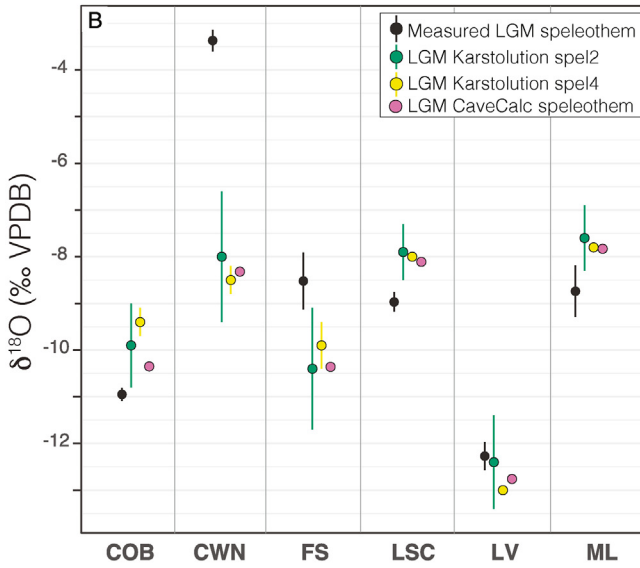
#### 4.1. Simulation comparison and potential biases

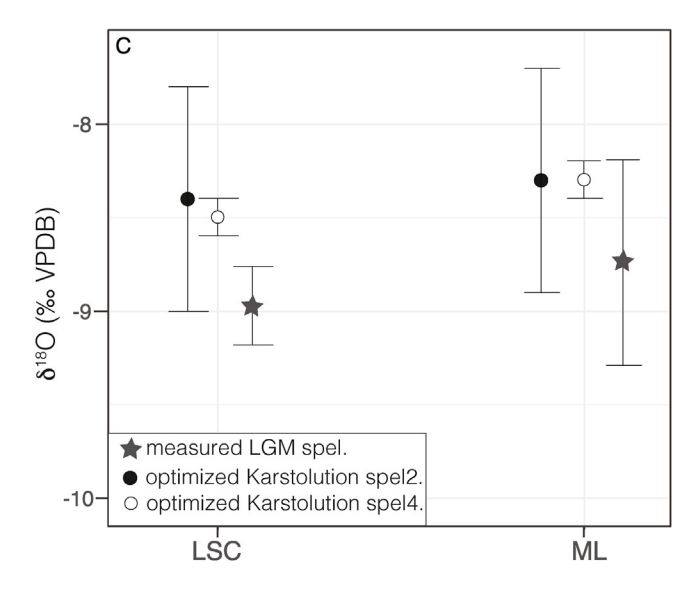
Our simulated pattern of hydrologic response at the LGM agrees with previous modeling works (e.g., Oster et al., 2015a; Lora et al., 2017; Morrill et al., 2018; Kageyama et al., 2021; Lofverstrom, 2020); the SW-US is generally wetter at the LGM and the NW-US is generally drier (Fig. 1). Although this work is, to the best of our knowledge, the first to explicitly track North Pacific ETCs at the LGM, many of the mechanisms driving the change in W-US moisture agree with previous hypotheses. Like prior research, we find an equatorward shift and increase in North Pacific cool season ETCs at the LGM (e.g., Yanase and Abe-Ouchi, 2007; Laîné et al., 2009, Fig. 5). As recognized in previous works, this ETC response appears to be associated with both an increased horizontal temperature gradient due to cooling and a southward deflection/intensification of the low-level jet due to the presence of North American ice sheets (e.g., Broccoli and Manabe, 1987; Wang et al., 2018, Fig. 8; Fig. 9). The results presented here further suggest that this increase in more southerly North Pacific ETCs during the cool season allows more ETCs to advect low-latitude moisture, resulting in nearmaintenance of present-day cool season moisture transport close to the southwest coast despite significantly lower total precipitable water at the LGM. This response is partly attributable to AR activity as found previously (Lora et al., 2017). We also identify an important role for thermodynamically driven hydroclimate changes in the W-US at the LGM (Fig. 6). The greater moisture removal efficiency due to an enhanced horizontal temperature gradient from the North Pacific to the US interior has been identified in previous studies (e.g., Boos, 2012; Wong et al., 2016; Morrill et al., 2018). However, these previous works were unable to confirm the role of cool season storm activity in maintaining moisture flux to the SW-

US at the LGM due to the use of lower temporal resolution model data. Finally, our findings support some previous speculation on the role of changes in seasonality and storminess (e.g., Santi et al., 2020), with an increase in relatively depleted cool season precipitation at the LGM in the Great Basin region.

From our sensitivity experiments, the moisture transport response to the W-US at the LGM is a product of both orographic and temperature changes (Fig. 8; Fig. 9). Although both factors increase cool season ETC activity in the North Pacific, colder terrestrial surface temperature during the LGM primarily increases moisture removal efficiency and only the response to LGM orography increases AR frequency. The impact of these drivers on W-US hydroclimate are dependent on somewhat uncertain boundary conditions. For example, our understanding of ice sheet topography has evolved significantly over the years (e.g., Abe-Ouchi et al., 2015). The spatial extent of the Laurentide ice sheet is well constrained by geological data, but the thickness and topographic elevation is more uncertain; the elevation of the ICE-6G topography used here is not as pronounced as the ICE-5G topography (e.g., Peltier et al., 2015). Our results suggest that a more prominent Laurentide ice sheet, such as ICE-5G, may further displace south and increase cool season ETC and AR activity in the North Pacific, as proposed by Löfverström et al. (2016). This may help explain the somewhat muted SW-US hydrologic response at the LGM in our and PMIP4 simulations relative to the mean from older PMIP simulations. Relatedly, we suspect that the amount of moisture transport is dependent on the Earth system sensitivity of the climate model. Although CESM1 has a non-linear Earth system sensitivity that generally performs well in paleoclimate simulations (e.g., Zhu et al., 2019; Feng et al., 2020), the LGM simulation presented here is cooler (7.3 °C global surface cooling relative to PI) than many other Earth system models and temperature reconstructions (e.g., Hargreaves et al., 2012; Shakun et al., 2012; Kageyama et al., 2021; Tierney et al., 2020). Regionally, we simulate 11.1 °C of cooling in the central Sierra Nevada foothills at the LGM, which is significantly greater than a recently derived noble gas temperature difference of  $5.2 \pm 1.7$  °C (Wortham et al., in review). The region, however, contains a strong temperature gradient associated with steep and heterogenous topography. Higher horizontal resolution is therefore necessary to better compare models and proxies in this region. More generally, if iCESM1.3 overestimates cooling at the LGM, it likely underestimates North Pacific moisture and moisture transport. Concurrently, LGM cooling amplifies land-sea temperature contrast, which increases moisture removal efficiency and reduces evaporation. Therefore, we cannot easily determine the hydroclimate and  $\delta^{18}O_p$  biases caused by a possible surface temperature bias in our LGM simulation. That said, we may expect more precipitation in the W-US in a warmer LGM climate based on the findings from our sensitivity experiments. Finally, AR activity is likely impacted by LGM temperature and moisture transport. Unlike ETCs, ARs do not have a universal definition (Shields et al., 2018). It is possible that the cold North Pacific surface temperature in our LGM simulation leads to bands of integrated vapor transport that do not reach the present-day-based threshold for classification as ARs (Lora et al., 2020). To an extent, we expect AR frequency to scale with background precipitable water and IVT based on our fixed parameters for AR identification. Techniques that use relative percentile IVT thresholds for AR detection may show an increase in AR frequency near the SW-US at the LGM (Rutz et al., 2019). When we reduce the thresholds for AR detection in TempestExtremes, we find an increase in AR frequency in parts of the North Pacific at the LGM relative to PI (Fig. S10). This is a topic that requires future study using different thresholds and AR detection algorithms.







#### 4.2. Interpreting proxies

Our simulations demonstrate that the general reduction in  $\delta^{18}O_n$ in the W-US at the LGM is complex, driven primarily by greater moisture removal efficiency and secondly by a greater portion of annual precipitation falling in the cool season months. These results agree well with the late glacial and LGM records of speleothem  $\delta^{18}$ O from the W-US and help to reconcile the various interpretations of these records. In the interior SW-US, the stalagmites from both FS and COB display more negative  $\delta^{18}$ O at the LGM than during the youngest part of the records, which is the end of the Younger Dryas (~11,500 years BP) (Fig. 2). In both cases, this shift to more negative speleothem  $\delta^{18}O$  during the LGM has been interpreted to reflect an increased contribution of relatively more negative cool season precipitation (Asmerom et al., 2010; Wagner et al., 2010). Consistent with this interpretation, our simulations show an increase in cool season precipitation across the study region, including the SW-US, at the LGM (Fig. 7b). For comparison, our estimated LGM drip water (Fig. 10a) computed for both FS and COB most closely aligns with mean annual  $\delta^{18}O_p$  from the iCESM1.3 experiments rather than wet season  $\delta^{18}O_{p.}$  Notably, for FS, the wettest 3-month period occurs in the summer for both the PI (MII) and the LGM (IJA), whereas at COB the wettest 3 month period occurs in the winter and early spring in both time slices (JFM).

In the Great Basin, more negative  $\delta^{18}O$  values during the late glacial compared to the Holocene in LV speleothems have been interpreted to reflect a combination of colder glacial temperatures and changes in atmospheric circulation that potentially altered moisture source or rainout history of air masses reaching the LV caves (Lachniet et al., 2014). Our simulations add more detail to this interpretation, as they demonstrate that the more negative LGM  $\delta^{18}O_p$  signal is a result of increased moisture removal efficiency and rainout, as well as changes in the relative amount of moisture from different sources at the site. Furthermore, the relative amount of simulated winter precipitation greatly increases at LV, which also contributes to the lower  $\delta^{18}O_p$  values. Like the SW-US caves, the estimated drip water from LV is also most closely aligned with mean annual rather than wet season (DJF)  $\delta^{18}O_p$  indicated by the iCESM1.3 simulation (Fig. 10a).

Neither of the California speleothem records, LSC or ML, extend into the Holocene. However, the ML records show good agreement with the  $\delta^{18}O$  record of the last deglaciation from nearby Moaning Cave (Oster et al., 2015b) which does extend into the early Holocene (Oster et al., 2009) and shows increasing  $\delta^{18}O$  values relative to the late glacial ML record. The LSC record shows increased  $\delta^{18}O$  values at the LGM relative to the deglacial part of that record (Fig. 2b), and both records display smaller changes in  $\delta^{18}O$  compared to the more inland LV, FS, and COB sites. These observations are consistent with our model results that show smaller negative or even positive  $\delta^{18}O_p$  anomalies at the LGM along the coast (Fig. 1a), and magnification of the negative  $\delta^{18}O_p$  inland as rainout increases. It has been hypothesized that increases in moisture from the CENP region at the

**Fig. 10.** Proxy-Model comparison. A) Comparison of amount weighted mean annual and wet season  $\delta^{18}O_p$  from the LGM simulation of iCESM1.3 with drip water estimated from LGM/late glacial speleothem  $\delta^{18}O$  using mean annual LGM temperature from iCESM1.3 and using the calcite-water oxygen isotope fractionation factors of Tremaine et al. (2011) and Kim and O'Neil (1997). B) Measured LGM/late glacial speleothem  $\delta^{18}O$  compared with pseudo-stalagmites forward modeled using CaveCalc (Owen et al., 2018) and Karstolution (Treble et al., 2019). Error bars on the estimated drip water values encompass the standard deviation of LGM/late glacial  $\delta^{18}O$  variability in the speleothem records (500–1000yr) and Karstolution time series. C) Comparison of measured LGM/late glacial speleothem  $\delta^{18}O$  with pseudo-stalagmites forward modeled with Karstolution, tuned using cave monitoring data for the California cave sites (LSC and ML). Error bars represent 1 standard deviation about the mean for the measured speleothem and Karstolution time series. See text for further description.

LGM, relative to moisture from the North Pacific could have contributed to the higher speleothem  $\delta^{18}O$  values at LSC (Oster et al., 2020). Indeed, our water tagging results suggest that moisture from the CENP does increase at the LGM, and the increase in nearby moisture from CENP at the expense of more depleted moisture from the north and west limits depletion along the coast despite increased moisture removal efficiency. At these more coastal sites, the mean annual and wet season  $\delta^{18}O_p$  values are very similar and within 0.5% of the estimated drip water values for both caves.

The largest discrepancy between measured speleothem  $\delta^{18}O$ during the late glacial and our model LGM results occurs at the CWN site in Texas. For this speleothem, late glacial  $\delta^{18}$ O and the drip water estimated from it are several per mil more positive than the simulated LGM  $\delta^{18}O_p$  from our iCESM1.3 experiments (Fig. 10a). Observations of rainfall from central Texas indicate that the primary source is the Gulf of Mexico (Pape et al., 2010), and the CWN stalagmite record has been interpreted primarily as a reflection of changing  $\delta^{18}\text{O}$  of Gulf of Mexico surface waters with melting of the Laurentide Ice Sheet (Feng et al., 2014). Our comparison of modern measured rainfall  $\delta^{18}$ O with modeled  $\delta^{18}$ O<sub>p</sub> from the PI simulation also suggests that measured precipitation is ~3% higher than the model output (Fig. S1). This suggests a model bias. Nusbaumer et al. (2017) show that iCESM1 overestimates deep convection, resulting in a negative bias in  $\delta^{18}O_p$ . Unlike the W-US, which receives most of its precipitation from synoptic systems during the cool season months, the CWN site receives a large portion of its annual precipitation from local convection during the spring and summer. This difference in portioning of precipitation type and season between regions may explain the depletion bias in iCESM1.3 at the CWN site. It is also possible that relatively enriched moisture from the Gulf of Mexico does not extend far enough inland in the model. Either way, higher model resolution raises  $\delta^{18}O_p$  at the CWN location by better resolving these features (Nusbaumer et al., 2017).

#### 4.3. Model-proxy comparison approaches

With the growing number of modeling groups running water isotope-enabled paleoclimate simulations, there is increased attention toward developing protocols for comparing isotopebased proxy records to climate model output. Comas-Bru et al. (2019) proposed methods for comparing speleothem  $\delta^{18}$ O to water isotope-enabled model output, focusing on evaluating isotope anomalies between time slices and spatial patterns of variability between records and models in a given time slice. As most W-US speleothem records do not extend from the LGM to the present, precluding our ability to calculate anomalies, we focused on evaluating approaches for comparing the LGM speleothem  $\delta^{18}$ O to the LGM iCESM1.3 output across this region. Following the strategy outlined in Comas-Bru et al. (2019), we computed estimated drip water values from the measured speleothem  $\delta^{18}O$  and the modeled LGM temperature, evaluating both the Tremaine et al. (2011) empirical isotope fractionation factor and the equilibrium fractionation relationship of Kim and O'Neil (1997). Our results suggest that this approach of estimating LGM drip water results in a reasonable comparison with modeled  $\delta^{18}O_{p.}$  At most of our sites the estimated drip water value and the modeled  $\delta^{18}O_p$  agree within ~0.5%. Further, there is no clear evidence that one fractionation factor leads to closer agreement between the drip water estimates and modeled  $\delta^{18}O_p$  (Fig. 10a). That said, the Kim and O'Neil (1997) equation consistently produces estimated drip water values that are higher and more fractionated from speleothem  $\delta^{18}\text{O}$  values than the Tremaine et al. (2011) relationship.

Our results do suggest that applying a proxy forward model to the climate model output supports robust comparisons between speleothem proxies and models, particularly for sites where the cave system is well characterized by monitoring data. Despite slightly different approaches, the two forward proxy models we utilized, CaveCalc and Karstolution, produce similar results, which is encouraging (Fig. 10b). One advantage of the Karstolution forward model is that it inputs the full time-series of climate model information for a given period, allowing evaluation of the influence of mixing and water storage in the karst aguifer on the forwardmodeled speleothem  $\delta^{18} O_{p.}$  Although the time frame of the climate model output and Karstolution forward-modeled speleothem  $\delta^{18}$ O time series (Fig. S3) is much shorter than the amount of time included in our speleothem LGM estimates (500–1000 years), the forward-modeled speleothem time-series does support an evaluation of the temporal variability on a limited timescale as well as an assessment of the potential influence of seasonality on these records. An understanding of seasonal cave ventilation from monitoring can improve future proxy-model comparison as the Karstolution model can be appropriately tuned. Likewise, an understanding of water-residence time in the epikarst of the cave(s) of interest can help determine which forward-modeled stalagmite is the more appropriate comparison. However, our results also demonstrate that when cave monitoring data are not available, both Karstolution and CaveCalc produce reasonable comparisons with the measured speleothem values using default settings. Further, if monthly time-series are not available as climate model output, CaveCalc, which accepts mean annual values for the necessary parameters, also produces reasonable results.

#### 4.4. Final thoughts: reconciling existing mechanisms for the W-US

Putting our findings in the context of prior hypotheses, we find that the hydroclimate response in the W-US at the LGM is the result of several previously identified mechanisms. Like prior studies, we observe a southward displacement and intensification of the North Pacific low-level jet stream, driven primarily by the presence of LGM ice sheets (e.g., Wang et al., 2018). Extratropical cyclone activity associated with a stronger latitudinal surface temperature gradient and enhanced jet in the North Pacific leads to a greater number of more southerly storms impacting the W-US at the LGM during the cool season months (Nov-Mar; e.g., Laîné et al., 2009). As a result of these factors, cool season moisture transport into the SW-US is only slightly reduced, despite significantly less atmospheric water vapor due to cooler temperatures at the LGM. AR activity also plays a role in maintaining SW-US moisture transport at the LGM but the magnitude of contribution likely depends on AR identification choices (e.g., Lora et al., 2017). In the SW-US, continued moisture input from the subtropics in combination with greater moisture removal efficiency from increased land-sea temperature contrast leads to enhanced cool season precipitation at the LGM (e.g., Boos, 2012); reduced evaporation enhances this moistening. In the NW-US, the reduction in atmospheric water vapor and its transport by the low-level jet and ETCs, in concert with entrainment of dry, stable air from the North American ice sheets, results in reduced precipitation at LGM during the cool season. In addition, summer precipitation generally decreases in the W-US at the LGM, especially in regions with significant convective precipitation. Overall, this combination of dynamic and thermodynamic changes at the LGM result in wetter conditions in the SW-US and drier conditions in the NW-US.

The simulated annual and cool season  $\delta^{18}O_p$  changes in the W-US at the LGM do not reflect the pattern of wetting and drying, but the mechanisms governing both are related. The  $\delta^{18}O_p$  changes at the LGM are primarily driven by responses in moisture removal efficiency followed by seasonality, with greater moisture removal efficiency leading to isotopic depletion into the continental interior

and more cool season precipitation leading to isotopic depletion in the Great Basin region. Enhanced rainout at the LGM results in more depletion as moisture moves into the continental interior, which agrees with speleothem  $\delta^{18}$ O. In contrast, atmospheric circulation and moisture availability play a larger role in the precipitation responses in the W-US at the LGM. Understanding the mechanisms responsible for the differences between precipitation and  $\delta^{18}O_p$  can tell us about unique aspects of past climate change. Based on our results, speleothem  $\delta^{18}$ O records of the W-US may provide a distinct signature of climate change at the LGM, which complements other hydroclimate proxies such as lake and pollen records. Through appreciating the multitude of processes that impact water isotopic concentrations, we can produce a more complete picture of past hydroclimate change. Improved model resolution and surface boundary conditions will be important next steps for reconciling regionally variability found in proxy records of the W-US at the LGM.

#### **Author contributions**

C.T., M.L., J.O., B.W., C.dW., and I.M. conceived the study and designed the experiments; C.T. and ML setup the climate model experiments; C.T. performed the climate model experiments and analyzed the climate model outputs with input from all authors; J.O., B.W., C.dW., and I.M. compiled the speleothem records and performed the proxy forward model experiments; A.R. and C.Z. configured the TempestExtremes analyses; C.H. and Z.L. provided the iTraCE boundary conditions and model data; C.T. drafted the manuscript with contributions from M.L., J.O., B.W., C.dW., and I.M.; All authors discussed the results and contributed to the final manuscript.

#### **Funding**

This work was supported by NSF grants AGS-1804747 to Tabor and Montañez, AGS-1554998 to Oster, and AGS-1810682 to Liu.

#### **Declaration of competing interest**

The authors declare that they have no known competing financial interests or personal relationships that could have appeared to influence the work reported in this paper.

#### Acknowledgements

The CESM project is supported primarily by the National Science Foundation (NSF). This material is based upon work supported by the National Center for Atmospheric Research (NCAR), which is a major facility sponsored by the NSF under Cooperative Agreement No. 1852977. Computing and data storage resources, including the Cheyenne supercomputer (https://doi.org/10.5065/DGRX99HX), were provided by the Computational and Information Systems Laboratory (CISL) at NCAR. The iCESM1.2 code is publicly available at https://github.com/NCAR/iCESM1.2. Data used in this manuscript are archived on NCAR Campaign Storage and UConn HPC. Additional data used in this manuscript may be requested from the authors. We thank Juan Lora for discussion about and assistance with atmospheric river tracking. We thank editor Ingrid Hendy for handling our manuscript and the thoughtful comments of two anonymous reviewers.

#### Appendix A. Supplementary data

Supplementary data to this article can be found online at https://doi.org/10.1016/j.quascirev.2021.107255.

#### References

- Abe-Ouchi, A., Saito, F., Kageyama, M., Braconnot, P., Harrison, S.P., Lambeck, K., Takahashi, K., 2015. Ice-sheet configuration in the CMIP5/PMIP3 last glacial maximum experiments. Geosci. Model Dev. (GMD) 8 (11), 3621–3637.
- Asmerom, Y., Polyak, V.J., Burns, S.J., 2010. Variable winter moisture in the southwestern United States linked to rapid glacial climate shifts. Nat. Geosci. 3 (2), 114–117
- Baker, A., Bradley, C., 2010. Modern stalagmite  $\delta$ 180: instrumental calibration and forward modelling. Global Planet. Change 71 (3–4), 201–206.
- Baker, A., Bradley, C., Phipps, S.J., Fischer, M., Fairchild, I.J., Fuller, L., Azcurra, C., 2012. Millennial-length forward models and pseudoproxies of stalagmite  $\delta$  18 O: an example from NW Scotland. Clim. Past 8 (4), 1153–1167.
- Baker, A.J., Mattey, D.P., Baldini, J.U., 2014. Reconstructing modern stalagmite growth from cave monitoring, local meteorology, and experimental measurements of dripwater films. Earth Planet Sci. Lett. 392, 239–249.
- Bartlein, P.J., Harrison, S.P., Brewer, S., Connor, S., Davis, B.A.S., Gajewski, K., Wu, H., 2011. Pollen-based continental climate reconstructions at 6 and 21 ka: a global synthesis. Clim. Dynam. 37 (3), 775–802.
- Bereiter, B., Eggleston, S., Schmitt, J., Nehrbass-Ahles, C., Stocker, T.F., Fischer, H., Chappellaz, J., 2015. Revision of the EPICA Dome C CO2 record from 800 to 600 kyr before present. Geophys. Res. Lett. 42 (2), 542–549.
- Bhattacharya, T., Tierney, J.E., DiNezio, P., 2017. Glacial reduction of the North American Monsoon via surface cooling and atmospheric ventilation. Geophys. Res. Lett. 44 (10), 5113–5122.
- Boos, W.R., 2012. Thermodynamic scaling of the hydrological cycle of the last glacial maximum. J. Clim. 25 (3), 992–1006.
- Bradley, C., Baker, A., Jex, C.N., Leng, M.J., 2010. Hydrological uncertainties in the modelling of cave drip-water δ18O and the implications for stalagmite palae-oclimate reconstructions. Quat. Sci. Rev. 29 (17−18), 2201−2214.
- Brady, E., Stevenson, S., Bailey, D., Liu, Z., Noone, D., Nusbaumer, J., Zhu, J., 2019. The connected isotopic water cycle in the Community Earth System Model version 1. J. Adv. Model. Earth Syst. 11 (8), 2547–2566.
- Broccoli, A.J., Manabe, S., 1987. The influence of continental ice, atmospheric CO 2, and land albedo on the climate of the last glacial maximum. Clim. Dynam. 1 (2), 87–99.
- Chang, E.K., Zheng, C., Lanigan, P., Yau, A.M., Neelin, J.D., 2015. Significant modulation of variability and projected change in California winter precipitation by extratropical cyclone activity. Geophys. Res. Lett. 42 (14), 5983–5991.
- Cohmap Members, 1988. Climatic changes of the last 18,000 years: observations and model simulations. Science 1043–1052.
- Comas-Bru, L., Harrison, S.P., Werner, M., Rehfeld, K., Scroxton, N., Veiga-Pires, C., 2019. Evaluating model outputs using integrated global speleothem records of climate change since the last glacial. Clim. Past 15 (4), 1557—1579.
- Comas-Bru, L., Atsawawaranunt, K., Harrison, S., 2020. SISAL (Speleothem Isotopes Synthesis and Analysis Working Group) Database, version 2.0.
- Deininger, M., Fohlmeister, J., Scholz, D., Mangini, A., 2012. Isotope disequilibrium effects: the influence of evaporation and ventilation effects on the carbon and oxygen isotope composition of speleothems—A model approach. Geochem. Cosmochim. Acta 96, 57–79.
- Dettinger, M.D., Cayan, D.R., Diaz, H.F., Meko, D.M., 1998. North—south precipitation patterns in western North America on interannual-to-decadal timescales. J. Clim. 11 (12), 3095—3111.
- Dettinger, M., Udall, B., Georgakakos, A., 2015. Western water and climate change. Ecol. Appl. 25 (8), 2069–2093.
- Diffenbaugh, N.S., Swain, D.L., Touma, D., 2015. Anthropogenic warming has increased drought risk in California. Proc. Natl. Acad. Sci. Unit. States Am. 112 (13), 3931–3936.
- Duplessy, J.C., Labeyrie, L., Waelbroeck, C., 2002. Constraints on the ocean oxygen isotopic enrichment between the last glacial maximum and the Holocene: paleoceanographic implications. Quat. Sci. Rev. 21 (1–3), 315–330.
- Fairchild, I.J., Smith, C.L., Baker, A., Fuller, L., Spötl, C., Mattey, D., McDermott, F., 2006. Modification and preservation of environmental signals in speleothems. Earth Sci. Rev. 75 (1–4), 105–153.
- Feakins, S.J., Wu, M.S., Ponton, C., Tierney, J.E., 2019. Biomarkers reveal abrupt switches in hydroclimate during the last glacial in southern California. Earth Planet Sci. Lett. 515, 164–172.
- Feng, W., Casteel, R.C., Banner, J.L., Heinze-Fry, A., 2014. Oxygen isotope variations in rainfall, drip-water and speleothem calcite from a well-ventilated cave in Texas, USA: assessing a new speleothem temperature proxy. Geochem. Cosmochim. Acta 127, 233—250.
- Feng, R., Otto-Bliesner, B.L., Brady, E.C., Rosenbloom, N., 2020. Increased climate response and earth system sensitivity from CCSM4 to CESM2 in mid-Pliocene simulations. J. Adv. Model. Earth Syst. 12 (8), e2019MS002033.
- Guan, B., Waliser, D.E., 2015. Detection of atmospheric rivers: evaluation and application of an algorithm for global studies. J. Geophys. Res.: Atmosphere 120 (24), 12514–12535.
- Guo, Y., Shinoda, T., Guan, B., Waliser, D.E., Chang, E.K., 2020. Statistical relationship between atmospheric rivers and extratropical cyclones and anticyclones. J. Clim. 33 (18), 7817–7834.
- Hamlet, A.F., Lettenmaier, D.P., 2007. Effects of 20th century warming and climate variability on flood risk in the western US. Water Resour. Res. 43 (6).
- Hargreaves, J.C., Annan, J.D., Yoshimori, M., Abe-Ouchi, A., 2012. Can the last glacial maximum constrain climate sensitivity? Geophys. Res. Lett. 39 (24).

- He, C., Liu, Z., Otto-Bliesner, B.L., Brady, E.C., Zhu, C., Tomas, R., Bao, Y., 2021. Hydroclimate footprint of pan-Asian monsoon water isotope during the last deglaciation. Sci. Adv. 7 (4), eabe2611.
- Hudson, A.M., Hatchett, B.J., Quade, J., Boyle, D.P., Bassett, S.D., Ali, G., Marie, G., 2019. North-south dipole in winter hydroclimate in the western United States during the last deglaciation. Sci. Rep. 9 (1), 1–12.
- Hurrell, J.W., Holland, M.M., Gent, P.R., Ghan, S., Kay, J.E., Kushner, P.J., Marshall, S., 2013. The community earth system model: a framework for collaborative research. Bull. Am. Meteorol. Soc. 94 (9), 1339–1360.
- Kageyama, M., Albani, S., Braconnot, P., Harrison, S.P., Hopcroft, P.O., Ivanovic, R.F., Zheng, W., 2017. The PMIP4 contribution to CMIP6—Part 4: scientific objectives and experimental design of the PMIP4-CMIP6 Last Glacial Maximum experiments and PMIP4 sensitivity experiments. Geosci. Model Dev. (GMD) 10 (11), 4035—4055.
- Kageyama, M., Harrison, S.P., Kapsch, M.L., Lofverstrom, M., Lora, J.M., Mikolajewicz, U., Zhu, J., 2021. The PMIP4 Last Glacial Maximum experiments: preliminary results and comparison with the PMIP3 simulations. Clim. Past 17 (3), 1065–1089.
- Kim, S.T., O'Neil, J.R., 1997. Equilibrium and nonequilibrium oxygen isotope effects in synthetic carbonates. Geochem. Cosmochim. Acta 61 (16), 3461–3475.
- Kottek, M., Grieser, J., Beck, C., Rudolf, B., Rubel, F., 2006. World Map of the Köppen-Geiger Climate Classification Updated.
- Lachniet, M.S., Denniston, R.F., Asmerom, Y., Polyak, V.J., 2014. Orbital control of western North America atmospheric circulation and climate over two glacial cycles. Nat. Commun. 5 (1), 1–8.
- Laîné, A., Kageyama, M., Salas-Mélia, D., Voldoire, A., Riviere, G., Ramstein, G., Peterschmitt, J.Y., 2009. Northern hemisphere storm tracks during the last glacial maximum in the PMIP2 ocean-atmosphere coupled models: energetic study, seasonal cycle, precipitation. Clim. Dynam. 32 (5), 593–614.
- Laskar, J., Fienga, A., Gastineau, M., Manche, H., 2011. La2010: a new orbital solution for the long-term motion of the Earth. Astron. Astrophys. 532, A89.
- LeGrande, A.N., Schmidt, G.A., 2006. Global gridded data set of the oxygen isotopic composition in seawater. Geophys. Res. Lett. 33 (12).
- Lofverstrom, M., 2020. A dynamic link between high-intensity precipitation events in southwestern North America and Europe at the Last Glacial Maximum. Earth Planet Sci. Lett. 534, 116081.
- Löfverström, M., Liakka, J., 2016. On the limited ice intrusion in Alaska at the LGM. Geophys. Res. Lett. 43 (20), 11–30, 0.
- Löfverström, M., Caballero, R., Nilsson, J., Messori, G., 2016. Stationary wave reflection as a mechanism for zonalizing the Atlantic winter jet at the LGM. J. Atmos. Sci. 73 (8), 3329–3342.
- Lora, J.M., 2018. Components and mechanisms of hydrologic cycle changes over north America at the last glacial maximum. J. Clim. 31 (17), 7035–7051.
- Lora, J.M., Mitchell, J.L., Risi, C., Tripati, A.E., 2017. North Pacific atmospheric rivers and their influence on Western North America at the last glacial maximum. Geophys. Res. Lett. 44 (2), 1051–1059.
- Lora, J.M., Shields, C.A., Rutz, J.J., 2020. Consensus and disagreement in atmospheric river detection: ARTMIP global catalogues. Geophys. Res. Lett. 47 (20), e2020GL089302.
- Lyle, M., Heusser, L., Ravelo, C., Yamamoto, M., Barron, J., Diffenbaugh, N.S., Andreasen, D., 2012. Out of the tropics: the pacific, Great Basin lakes, and late pleistocene water cycle in the western United States. Science 337 (6102), 1629–1633.
- Manabe, S., Broccoli, A.J., 1985. The influence of continental ice sheets on the climate of an ice age. J. Geophys. Res.: Atmosphere 90 (D1), 2167–2190.
- McGee, D, Moreno-Chamarro, E, Marshall, J, Galbraith, E, 2018. Western US lake expansions during Heinrich stadials linked to Pacific Hadley circulation. Sci. Adv. https://doi.org/10.1126/sciadv.aav0118.
- Morrill, C., Lowry, D.P., Hoell, A., 2018. Thermodynamic and dynamic causes of pluvial conditions during the Last Glacial Maximum in western North America. Geophys. Res. Lett. 45 (1), 335–345.
- Nusbaumer, J., Wong, T.E., Bardeen, C., Noone, D., 2017. Evaluating hydrological processes in the C ommunity A tmosphere M odel V ersion 5 (C AM5) using stable isotope ratios of water. J. Adv. Model. Earth Syst. 9 (2), 949–977.
- Oster, J.L., Kelley, N.P., 2016. Tracking regional and global teleconnections recorded by western North American speleothem records. Quat. Sci. Rev. 149, 18–33.
- Oster, J.L., Montañez, I.P., Sharp, W.D., Cooper, K.M., 2009. Late Pleistocene California droughts during deglaciation and Arctic warming. Earth Planet Sci. Lett. 288 (3–4), 434–443.
- Oster, J.L., Montañez, I.P., Kelley, N.P., 2012. Response of a modern cave system to large seasonal precipitation variability. Geochem. Cosmochim. Acta 91, 92–108.
- Oster, J.L., Ibarra, D.E., Winnick, M.J., Maher, K., 2015a. Steering of westerly storms over Western North America at the last glacial maximum. Nat. Geosci. 8 (3), 201–205.
- Oster, J.L., Montanez, I.P., Santare, L.R., Sharp, W.D., Wong, C., Cooper, K.M., 2015b. Stalagmite records of hydroclimate in central California during termination 1. Quat. Sci. Rev. 127, 199–214.
- Oster, J.L., Warken, S.F., Sekhon, N., Arienzo, M.M., Lachniet, M., 2019. Speleothem paleoclimatology for the caribbean, Central America, and north America. Quaternary 2 (1), 5.
- Oster, J.L., Weisman, I.E., Sharp, W.D., 2020. Multi-proxy stalagmite records from northern California reveal dynamic patterns of regional hydroclimate over the last glacial cycle. Quat. Sci. Rev. 241, 106411.
- Owen, R., Day, C.C., Henderson, G.M., 2018. CaveCalc: a new model for speleothem chemistry & isotopes. Comput. Geosci. 119, 115–122.

- Pape, J.R., Banner, J.L., Mack, L.E., Musgrove, M., Guilfoyle, A., 2010. Controls on oxygen isotope variability in precipitation and cave drip waters, central Texas, USA. J. Hydrol. 385 (1–4), 203–215.
- Pausata, F.S., Löfverström, M., 2015. On the enigmatic similarity in Greenland δ180 between the oldest and younger Dryas. Geophys. Res. Lett. 42 (23), 10−470.
- Pausata, F.S., Battisti, D.S., Nisancioglu, K.H., Bitz, C.M., 2011. Chinese stalagmite δ 18 O controlled by changes in the Indian monsoon during a simulated Heinrich event. Nat. Geosci. 4 (7), 474–480.
- Peltier, W.R., Argus, D.F., Drummond, R., 2015. Space geodesy constrains ice age terminal deglaciation: the global ICE-6G\_C (VM5a) model. J. Geophys. Res.: Solid Earth 120 (1), 450–487.
- Rehfeld, K., Hébert, R., Lora, J.M., Lofverstrom, M., Brierley, C.M., 2020. Variability of surface climate in simulations of past and future. Earth System Dynamics 11 (2), 447–468.
- Rhoades, A.M., Jones, A.D., Srivastava, A., Huang, H., O'Brien, T.A., Patricola, C.M., Zhou, Y., 2020. The shifting scales of western US landfalling atmospheric rivers under climate change. Geophys. Res. Lett. 47 (17), e2020GL089096. Rhoades, A.M., Risser, M.D., Stone, D.A., Wehner, M.F., Jones, A.D., 2021. Implications
- Rhoades, A.M., Risser, M.D., Stone, D.A., Wehner, M.F., Jones, A.D., 2021. Implications of warming on western United States landfalling atmospheric rivers and their flood damages. Weather Climate Exterm. 32, 100326.
- Routson, C.C., McKay, N.P., Kaufman, D.S., Erb, M.P., Goosse, H., Shuman, B.N., Ault, T., 2019. Mid-latitude net precipitation decreased with Arctic warming during the Holocene. Nature 568 (7750), 83–87.
- Rutz, J.J., Shields, C.A., Lora, J.M., Payne, A.E., Guan, B., Ullrich, P., Viale, M., 2019. The atmospheric river tracking method intercomparison project (ARTMIP): quantifying uncertainties in atmospheric river climatology. J. Geophys. Res.: Atmosphere 124 (24), 13777—13802.
- Santi, L.M., Arnold, A.J., Ibarra, D.E., Whicker, C.A., Mering, J.A., Lomarda, R.B., Tripati, A., 2020. Clumped isotope constraints on changes in latest Pleistocene hydroclimate in the northwestern Great Basin: lake Surprise, California. GSA Bulletin 132 (11–12), 2669–2683.
- Seager, R., Ting, M., Held, I., Kushnir, Y., Lu, J., Vecchi, G., Naik, N., 2007. Model projections of an imminent transition to a more arid climate in southwestern North America. Science 316 (5828), 1181–1184.
- Shakun, J.D., Clark, P.U., He, F., Marcott, S.A., Mix, A.C., Liu, Z., Bard, E., 2012. Global warming preceded by increasing carbon dioxide concentrations during the last deglaciation. Nature 484 (7392), 49–54.
- Shields, C.A., Rutz, J.J., Leung, L.Y., Ralph, F.M., Wehner, M., Kawzenuk, B., Nguyen, P., 2018. Atmospheric river tracking method intercomparison project (ARTMIP): project goals and experimental design. Geosci. Model Dev. (GMD) 11 (6), 2455–2474.
- Shields, C.A., Kiehl, J.T., Rush, W., Rothstein, M., Snyder, M.A., 2021. Atmospheric rivers in high-resolution simulations of the paleocene eocene thermal maximum (PETM). Palaeogeogr. Palaeoclimatol. Palaeoecol. 567, 110293.
- Skinner, C.B., Lora, J.M., Payne, A.E., Poulsen, C.J., 2020. Atmospheric river changes shaped mid-latitude hydroclimate since the mid-Holocene. Earth Planet Sci. Lett. 541, 116293.
- Swain, D.L., Langenbrunner, B., Neelin, J.D., Hall, A., 2018. Increasing precipitation volatility in twenty-first-century California. Nat. Clim. Change 8 (5), 427–433.
- Tabor, C.R., Otto-Bliesner, B.L., Brady, E.C., Nusbaumer, J., Zhu, J., Erb, M.P., Noone, D., 2018. Interpreting precession-driven δ18O variability in the South Asian monsoon region. J. Geophys. Res.: Atmosphere 123 (11), 5927–5946.
- Tierney, J.E., Zhu, J., King, J., Malevich, S.B., Hakim, G.J., Poulsen, C.J., 2020. Glacial cooling and climate sensitivity revisited. Nature 584 (7822), 569–573.
- Treble, P, Bradley, C, Wood, A, Baker, A, Jex, C, Fairchild, I, Gagan, M, Cowley, J, Azcurra, C, 2013. An isotopic and modelling study of flow paths and storage in Quaternary calcarenite, SW Australia: implications for speleothem paleoclimate records. Ouat. Sci. Rev.
- Treble, P., Mah, M., Griffiths, A.D., Baker, A., Deininger, M., Kelly, B., Hankin, S., 2019. Separating Isotopic Impacts of Karst and In-Cave Processes from Climate Variability Using an Integrated Speleothem Isotope-Enabled Forward Model.
- Tremaine, D.M., Froelich, P.N., Wang, Y., 2011. Speleothem calcite farmed in situ: modern calibration of δ18O and δ13C paleoclimate proxies in a continuously-monitored natural cave system. Geochem. Cosmochim. Acta 75 (17), 4929–4950.
- Ullrich, P.A., Zarzycki, C.M., 2017. TempestExtremes: a framework for scale-insensitive pointwise feature tracking on unstructured grids. Geosci. Model Dev. (GMD) 10 (3), 1069–1090.
- Ullrich, P.A., Zarzycki, C.M., McClenny, E.E., Pinheiro, M.C., Stansfield, A.M., Reed, K.A., 2021. TempestExtremes v2. 1: a community framework for feature detection, tracking and analysis in large datasets. Geosci. Model Dev. Discuss. (GMDD) 1–37.
- US Bureau of Economic Analysis, 2020. Gross Domestic Product by State, 4th Quarter and Annual 2020.
- US Census Bureau, 2020. Population, Population Change, and Estimated Components of Population Change. April 1, 2010 to July 1, 2019.
- Wagner, J.D., Cole, J.E., Beck, J.W., Patchett, P.J., Henderson, G.M., Barnett, H.R., 2010. Moisture variability in the southwestern United States linked to abrupt glacial climate change. Nat. Geosci. 3 (2), 110–113.
- Wang, N., Jiang, D., Lang, X., 2018. Northern westerlies during the last glacial maximum: results from CMIP5 simulations. J. Clim. 31 (3), 1135–1153.
- Wong, C.I., Potter, G.L., Montañez, I.P., Otto-Bliesner, B.L., Behling, P., Oster, J.L., 2016. Evolution of moisture transport to the western US during the last deglaciation. Geophys. Res. Lett. 43 (7), 3468–3477.
- Wortham, B.E., Mukhopadhyay, S., Montañez, I.P., Middleton, J., Tyra, A. in revision.

- A 5  $^{\circ}\text{C}$  cooling in Western Sierra Nevada, California, recorded in stalagmite noble gas concentrations during the Last Glacial Maximum. Earth Planet Sci. Lett..
- Yanase, W., Abe-Ouchi, A., 2007. The LGM surface climate and atmospheric circulation over East Asia and the North Pacific in the PMIP2 coupled model simulations. Clim. Past 3 (3), 439–451.
- Zarzycki, C.M., 2018. Projecting changes in societally impactful northeastern US snowstorms. Geophys. Res. Lett. 45 (21), 12–67, 0.
- Zhu, Y., Newell, R.E., 1998. A proposed algorithm for moisture fluxes from atmospheric rivers. Mon. Weather Rev. 126 (3), 725–735.
- Zhu, J., Liu, Z., Brady, E., Otto-Bliesner, B., Zhang, J., Noone, D., Tabor, C., 2017. Reduced ENSO variability at the LGM revealed by an isotope-enabled Earth system model. Geophys. Res. Lett. 44 (13), 6984–6992.
- system model. Geophys. Res. Lett. 44 (13), 6984–6992.
  Zhu, J., Poulsen, C.J., Tierney, J.E., 2019. Simulation of Eocene extreme warmth and high climate sensitivity through cloud feedbacks. Sci. Adv. 5 (9), eaax1874.